


Article

Long-Term Thermal Cycling Test and Heat-Charging Kinetics of Fe-Substituted Mn_2O_3 for Next-Generation Concentrated Solar Power Using Thermochemical Energy Storage at High Temperatures

Nobuyuki Gokon ^{1,2,*} , Kosuke Hayashi ², Hiroki Sawaguri ² and Fumiya Ohashi ²

¹ Program of Chemistry & Chemical Engineering, Faculty of Engineering, Niigata University, 8050 Ikarashi 2-Nocho, Niigata 950-2181, Japan

² Graduate School of Science and Technology, Niigata University, 8050 Ikarashi 2-Nocho, Niigata 950-2181, Japan; linguangyou4@gmail.com (K.H.); f21k004a@mail.cc.niigata-u.ac.jp (H.S.); f21b044a@mail.cc.niigata-u.ac.jp (F.O.)

* Correspondence: ngokon@eng.niigata-u.ac.jp; Tel.: +81-25-262-6820

Abstract: We studied the performance in terms of the long-term cyclic thermal storage and heat-charging kinetics of Fe-substituted manganese oxide for use in thermochemical energy storage at temperatures exceeding 550 °C in a next-generation concentrated solar power system in which a gas stream containing oxygen is used for reversible thermochemical processes. The Fe-substituted Mn_2O_3 was evaluated from the viewpoint of its microstructural characteristics, thermodynamic phase transitions, and long-term cycling stability. A kinetic analysis of the heat-charging mode was performed at different heating rates to formulate the kinetic equation and describe the reaction mechanism by determining the appropriate reaction model. Finally, the kinetics data for the sample obtained after the long-term cycling test were compared and evaluated with those of the as-prepared sample and kinetic literature data tested under different conditions. For the long-term cycled sample, the Avrami–Erofeev reaction model (An) with $n = 2$ describes the behavior of the first part of the charging mode, whereas the contracting area (R2) reaction model best fits the last half of the charging mode. For the as-prepared sample, except for the early stage of the charging mode (fractional conversion < 0.2), the contracting volume (R3) reaction model fits the charging mode over a fractional conversion range of 0.2–1.0 and the first-order (F1) reaction model fits in the fractional conversion range of 0.4–1.0. The predicted kinetic equations for both the samples were in good agreement with the experimental kinetic data.

Keywords: thermochemical energy storage; manganese oxides; Fe substitution; long-term thermal cycling; concentrated solar power



Citation: Gokon, N.; Hayashi, K.; Sawaguri, H.; Ohashi, F. Long-Term Thermal Cycling Test and Heat-Charging Kinetics of Fe-Substituted Mn_2O_3 for Next-Generation Concentrated Solar Power Using Thermochemical Energy Storage at High Temperatures. *Energies* **2022**, *15*, 4812. <https://doi.org/10.3390/en15134812>

Academic Editor: Antonio Rosato

Received: 10 June 2022

Accepted: 28 June 2022

Published: 30 June 2022

Publisher's Note: MDPI stays neutral with regard to jurisdictional claims in published maps and institutional affiliations.



Copyright: © 2022 by the authors. Licensee MDPI, Basel, Switzerland. This article is an open access article distributed under the terms and conditions of the Creative Commons Attribution (CC BY) license (<https://creativecommons.org/licenses/by/4.0/>).

1. Introduction

The increasing demand for renewable energy has led to solar energy being regarded as an infinite, sustainable, and clean energy source [1]. Among the various solar technologies, concentrated solar power (CSP) enables the production of dispatchable and potentially cost-effective renewable electricity from concentrated solar thermal power, which is traditionally used as a heat source for power generation via thermodynamic cycles [2]. To increase the feasibility of CSP and ultimately to achieve full autonomy from fossil fuels, the main challenge to overcome is the inherent intermittency in solar power generation [3]. Thus, efficient and low-cost energy storage remains a major technological challenge [4–6]. Thermal energy storage (TES) systems are essential for a global system with high penetration of solar energy to increase the flexibility of the electric grid and avoid the risks derived from transient peaks.

Several potential TES technologies for CSP plants have been proposed in recent years. These are based on three main concepts: sensible TES, in which solid or liquid media are used; latent TES, associated with phase changes in certain materials; and thermochemical energy storage (TCES) [7]. As the most mature of the three, sensible TES involves the use of various materials with high heat capacity, such as steam [8], molten salts [9–12], mineral oils [13], or ceramic materials [14]. Several commercial CSP plants that are operational or under construction store heat in molten salts or a steam accumulator to generate electricity overnight [15]. Latent TES, involving solid-to-liquid transitions, is an efficient alternative to sensible TES, owing to the higher storage capacities and small temperature differences between charging and discharging in comparison with sensible TES [16,17]. However, most latent TES systems based on inorganic salts and eutectic salts have low thermal conductivity, resulting in slow charging and discharging rates [18]. Thus, the heat transfer is enhanced by combining graphite finned tubes [19] and metal foam [20] with the inorganic salt-based phase change material (PCM). Another type of latent TES uses metallic alloy PCMs to improve the thermal conductivity, thermal response, and heat capacity [21–23]. However, metallic PCMs are limited in vacuum and inert atmospheres, and the encapsulation of metallic PCMs in temperature-resistant materials must be applied to avoid the oxidation of metallic PCMs at high temperatures [24,25].

This study focuses on the third concept, namely TCES. This method utilizes the heat from chemical reactions and is one of the most promising TES technologies, with the potential for higher energy efficiency than the other methods. Several reactions have been investigated for use in TCES, such as the calcination–carbonation process for calcium carbonate [26,27] and the redox process for metal oxides [28], both of which can be integrated into next-generation CSP plants that operate at temperatures > 550 °C. The TCES process, utilizing the reversible chemical reaction of a metal oxide, is expressed as follows:



The HC mode of a reversible chemical reaction is driven by the high-temperature heat provided by the concentrated solar radiation. This heat can be chemically stored (charged) as a reaction product in the reduced form, as shown in Equation (1). To release (discharge) the stored heat, the reduced oxide is oxidized back to $M_xO_y (s)$ in the reverse HD mode in a gas stream containing oxygen, as shown in Equation (2). The gas stream (inert gas, oxygen-lean gas, and air) is required to progress both modes, while the solid particles act as a thermochemical storage medium and heat transfer fluid (HTF), allowing operation temperatures > 550 °C in a next-generation CSP plant in the current study stage [29] in the United States. An open volumetric receiver [30] was developed and tested in the EU, which uses air as the HTF and metal oxide as the thermochemical storage medium. The use of a molten-salt [31] or liquid sodium [32] receiver in the central tower system of next-generation CSP plants can allow for operation at higher temperatures than the current state-of-the-art CSP plants. The main advantages of TCES are greater energy densities than sensible or latent TES systems, and the possibility of storing energy in a chemical form over a long time period and transporting it without significant loss [33].

The criteria for the choice of redox metal oxide to be used in TCES are the thermodynamics, working temperature, energy storage capacity, material costs, reaction kinetics, cyclical feasibility, toxicity to humans, and environmental safety. Wong extensively evaluated various metal oxides as TCES materials using a thermodynamic calculation and experimental analysis [28]. Among the oxides tested for TCES, BaO_2/BaO , Co_3O_4/CoO , Mn_2O_3/Mn_3O_4 , Fe_2O_3/Fe_3O_4 , and CuO/Cu_2O systems were proposed, investigated, and evaluated as possible materials for TCES. Several researchers have studied BaO_2/BaO [34–36], Co_3O_4/CoO [37–46], Mn_2O_3/Mn_3O_4 [47–52], Fe_2O_3/Fe_3O_4 [53], and CuO/Cu_2O systems [54] from the perspectives of thermodynamic analysis, redox

kinetics, repeatability, and reactor–heat exchangers. In addition, the perovskite family of oxides, with a chemical formula of ABO_3 , has been studied as a potential source for TCES because of the diverse thermochemical properties exhibited by the different elemental compositions that form large concentrations of vacancies in this type of structure [55–67]. Although the Co_3O_4/CoO system has good energy storage capacity, reaction kinetics, and cyclical feasibility, the material costs are a disadvantage. The Mn_2O_3/Mn_3O_4 system involves inexpensive materials but suffers from slow kinetics in its exothermic process (HD mode) and poor repeatability of the redox reaction in air under atmospheric pressure. The Fe_2O_3/Fe_3O_4 system, which involves low-cost materials, shows suitable kinetics for HC–HD modes, but has the drawbacks of extremely high temperatures (1392 °C in the HC mode and 1374 °C in the HD mode) and deactivation with redox cyclic tests due to severe sintering at high temperatures.

In order to utilize the advantages and compensate for the disadvantages of both the Mn_2O_3/Mn_3O_4 and Fe_2O_3/Fe_3O_4 systems, iron–manganese oxides of the $(Mn, Fe)_2O_3/(Mn, Fe)_3O_4$ systems, in which the iron is substituted as a secondary cation into manganese oxide, were developed and tested for TCES [50,53,65–69]. Carrillo et al. studied the influence of Fe's incorporation on the redox performance of the Mn_2O_3/Mn_3O_4 system [50]. Compared with the Mn_2O_3/Mn_3O_4 system, the Fe-substituted manganese oxides improved the oxygen production rate, as shown using a 30-cycle test at constant air flow. In particular, 20% Fe-substituted Mn_2O_3 exhibited the highest chemical energy storage density ($\Delta H_{red} = -219$ kJ/kg; $\Delta H_{ox} = +203$ kJ/kg). Block and Schmäcker examined the reaction enthalpy, temperature, and time for the 33%, 67%, and 83% Fe-substituted Mn_2O_3 at atmospheric pressure with an air flow [53]. The manganese-rich composition of the 33% Fe-substituted Mn_2O_3 system was reported as an interesting thermochemical storage material from the viewpoint of the highest enthalpies ($\Delta H_{red} = -233$ kJ/kg; $\Delta H_{ox} = +162$ kJ/kg), together with the low material costs. The kinetics and cyclic repeatability of 20% Fe-substituted Mn_2O_3 for HC and HD modes were investigated using a thermogravimetric analysis (TGA) [65]. The reaction enthalpy was $\Delta H_{ox} = +171$ kJ/kg at an average of 75 cycles. The master plots were used to analyze the kinetics of the HC mode using a non-isothermal heating mode under an inert Ar gas stream. Subsequently, the kinetics of the HD mode were analyzed in isothermal mode at constant temperatures under air flow. Woken et al. investigated the thermodynamics and kinetics of granular 25% Fe-substituted Mn_2O_3 prepared from technical-grade raw materials. The repeatability and reactivity were examined over 100 cycles in air using TGA. The kinetic models of the HC and HD modes were derived from experimental data under different oxygen partial pressures [66]. The reversible redox reaction of a granular technical-grade manganese–iron oxide was investigated for TCES at the laboratory scale by means of a packed-bed tube reactor [67]. André et al. experimentally studied the effect of Fe substitution in Mn_2O_3 in powder form using TGA, and compared this with thermodynamic calculations. The addition of Fe to Mn_2O_3 allows for the enhancement of the cycling stability above ~15 mol% Fe, with the suppression of any transition involving this tetragonal spinel phase [68]. Marziyeh et al. studied the reduction kinetics of submillimeter-sized spherical granular 67% Fe-substituted Mn_2O_3 . The kinetics were analyzed in the non-isothermal heating mode, under both inert Ar gas and an air stream, using TGA. The thermal analysis of the HC mode showed a reaction enthalpy of 200 kJ/kg under both atmospheres. A three-step shrinking core model has been proposed and used to describe the effective kinetics of the HC mode [69].

The authors studied the TCES thermal performance in terms of improving and evaluating non-substituted and 10–50% Fe-substituted manganese, as well as the perovskite family of redox oxides, by means of a TGA reactor at the laboratory scale [52]. The impacts of the operating temperature for Fe-substituted Mn_2O_3/Mn_3O_4 redox oxides were examined for two-step thermochemical cycles from the perspective of the redox temperatures and thermochemical storage capacity. In addition, certain Fe-X-substituted manganese oxides were examined to improve the reaction rate, short-term cycling stability, storage capacity, and redox temperatures [52]. However, the effects of the long-term thermal cycling stability

on TCES to assume 1-year operation have not been studied and evaluated for Fe-substituted Mn_2O_3 . It is considered that long-term thermal cycling may cause a morphological change in the sample in comparison to the as-prepared sample, affecting the kinetics of the HC–HD modes with oxygen release and absorption. In this study, the long-term thermal cycling stability of 20 mol% Fe-substituted Mn_2O_3 in 360 runs of HC–HD modes was evaluated in terms of the repeatability and stability from the perspective of the microstructural characteristics and thermodynamic phase transitions. The kinetic analysis of the HC mode for the sample subjected to the long-term thermal cycling test with a temperature swing under constant oxygen partial pressure was studied and compared with that of the as-prepared sample. Finally, the kinetic results in the present study were compared with the kinetic equations formulated under various test conditions in previous reports.

2. Materials and Methods

2.1. Preparation and Evaluation of Redox Material

The reagents $\text{Mn}(\text{NO}_3)_2 \cdot 6\text{H}_2\text{O}$ (98.0%) and $\text{Fe}(\text{NO}_3)_3 \cdot 9\text{H}_2\text{O}$ (99.0%) were purchased from Wako Pure Chemical Industries, Ltd. (Osaka, Japan), and Kanto Chemical Co., Inc. (Tokyo, Japan), respectively, and used without further purification. The oxide was prepared using these reagents via a modified Pechini process [52]. Briefly, stoichiometric quantities of metal nitrate reagents (0.04 mol) were dissolved in deionized distilled water (200 mL). Ethylene glycol (99.5%; Wako Pure Chemical Industries, Ltd.) and citric acid (98.0%, 0.02 mol; Wako Pure Chemical Industries, Ltd.) were added to the aqueous solution. The solution was stirred and heated at 80 °C for 1 h in an oil bath. Ethylene glycol (0.02 mol) was then added to the solution. The resulting solution was stirred and heated to 170 °C for 0.5 h in an oil bath for gel formation. The gel was moved to an alumina crucible and dried at 180 °C for 4.5 h using an electric heater. The resulting samples were ground using a mortar and pestle. The resulting black powder (precursor) was calcined at 900 °C for 8 h in an air stream (200 mL/min) heated using an electric heater.

The crystallographic phases were identified using powder X-ray diffraction (XRD; D2Phaser, Bruker, MA, USA) with Cu-K_α radiation ($2\theta = 20\text{--}80^\circ$). The step size and rate were fixed at 0.02° and 1 s per step, respectively. The crystalline phases were identified by comparison with standard reference patterns in an open-access repository (Crystallography Open Database, COD). The lattice parameters were evaluated through Rietveld refinement of the structural models using the whole-pattern fitting method from the FullProf package.

The morphology and particle size of the synthesized and long-term cycled samples were observed using a scanning electron microscope (SEM; JCM-6000, JEOL, Tokyo, Japan) operated at 15 kV. Before the SEM observation, a small amount of sample was coated as a pretreatment via gold evaporation to enhance the conductivity and avoid charge build-up during the observation.

2.2. Long-Term Thermal Cycling Stability Test in Non-Isothermal Charge/Discharge Modes

The Fe-substituted manganese oxide was tested for the thermochemical cycle, which comprised an HC mode to release oxygen from the oxide into the gas stream and a subsequent HD mode to absorb oxygen into the oxide from the gas stream containing oxygen. The experimental setup for the HC and HD modes of the thermochemical cycle was as follows. Approximately 50 mg of sample was packed into a platinum–rhodium cup (5.2 mm in diameter and 5.1 mm deep) and mounted on the balance point in the tubular ceramic chamber of the reactor. The sample mounted in the TGA reactor (STA2500 Regulus, NETZSCH, Selb, Germany; weight resolution of 0.03 μg , temperature resolution of 0.3 K) equipped for the differential thermal analysis (DTA) with a type S thermocouple (temperature resolution of $\pm 0.0025 \times |t|$ °C) was first heated to 1050 °C at a heating rate of 15 °C/min using an electric furnace, while passing a gas mixture ($P_{\text{O}_2} = 0.168$ bar) of synthetic air and high purity N_2 (99.999%, 5 N) through the reactor at a 250 sccm flow rate (standard $\text{cm}^3 \text{min}^{-1}$), controlled by a digital mass flow controller, in order to perform the HC mode. The synthetic gas was passed through the balance of the TGA reactor, whereas high-purity N_2 gas was

flowed into the control port of the balance mechanism to protect it from oxidation. The sample was cooled to 700 °C to perform the HD mode. The change in the mass of the sample caused by O₂ release during the HC mode and absorption during the HD mode were measured with respect to time. The HC and HD modes were alternately repeated for 360 runs, composed of three sets of 120 runs between 700 and 1050 °C to evaluate the long-term cyclability and thermal stability of the sample.

2.3. Kinetic Analysis of Non-Isothermal HC Mode for the Long-Term Cycled Sample

A kinetic analysis of the non-isothermal HC mode for the sample obtained after the long-term cycling stability test was performed using a TGA reactor. The sample mounted in the TGA reactor was first heated to 800 °C and then maintained at this temperature for 2 h to eliminate adsorptive species on the surface of the sample, such as water, CO₂, and O₂. Subsequently, the sample was heated to 1100 °C at different heating rates of 5–20 K/min using an electric furnace, while passing the gas stream through the reactor at a 250 sccm flow rate (standard cm³ min⁻¹) controlled by a digital mass flow controller to perform the HC mode. To complete the HC mode, the sample was maintained at 1100 °C for 20 min. After the HC mode, the sample was cooled to 800 °C at a cooling rate of 20 K/min and then maintained at this temperature for 2 h to proceed the oxidation reaction as much as possible and approach the reduction extent of the sample to zero (HD mode). The HC–HD mode was continuously performed at different heating rates of the order of 5, 10, 12, 15, and 20 K/min and a cooling rate of 20 K/min to acquire kinetic data for the HC mode of the sample.

The kinetics of the HC mode were analyzed and evaluated using non-isothermal master plots for various constant heating rates $\left(\frac{dT}{dt}\right)$. The characteristic feature of this method is the identification of appropriate reaction models from the actual reaction mechanisms by determining the activation energy using Arrhenius plots.

The fractional conversion of α in the solid reactant over the course of the reaction is defined as follows:

$$\alpha = \frac{m_i - m_t}{m_i - m_f}, \quad (3)$$

where m_i and m_f are the initial and final masses, respectively, and m_t is the mass of the sample at time t . In the TGA, the value of α for the thermochemical cycle of the HC mode was calculated using the measured change in the mass of the sample.

An isoconversion method was used to determine the Arrhenius parameters for the HC mode involving O₂ release from TGA data [70]. The isoconversion method is known for its reliability and wide applicability because the two prerequisites required for its formulation are independent of the reaction mechanism. The prerequisites for the rate of a chemical reaction are generally described using a fundamental equation for the isoconversion method:

$$\frac{d\alpha}{dt} = A \cdot \exp\left(-\frac{E_a}{RT}\right) \cdot f(\alpha) = k(T)f(\alpha), \quad (4)$$

where A and E_a correspond to the Arrhenius pre-exponential factor and apparent activation energy for the reaction, respectively; R is the gas constant; $k(T)$ is the rate parameter at temperature T ; and $f(\alpha)$ is a function of α , representing the so-called reaction model, which depends on the reaction mechanism.

The generalized time θ , which is the basic parameter for determining α , is defined as follows:

$$\theta = \int_0^t \exp\left(-\frac{E_a}{RT}\right) \cdot dt. \quad (5)$$

In the non-isothermal kinetic analysis involving the O₂ release process, different heating rates (HC mode) were applied. The same generalized time θ with different rate

conditions corresponds to the same value of α for the reaction, and vice versa. Thus, the generalized time of θ depends on α , and the time derivative of Equation (5) leads to:

$$\frac{d\theta}{dt} = \exp\left(-\frac{E_a}{RT}\right). \tag{6}$$

The following Equation (7) can be obtained from Equations (4) and (6):

$$\frac{d\alpha}{d\theta} = \frac{d\alpha}{dt} \times \frac{dt}{d\theta} = \frac{d\alpha}{dt} \times \exp\left(\frac{E_a}{RT}\right) = A \times f(\alpha). \tag{7}$$

Thus, the analytic equation for non-isothermal master plots leads to:

$$\frac{d\alpha/d\theta}{(d\alpha/d\theta)_{\alpha=0.5}} = \frac{f(\alpha)}{f(\alpha)_{\alpha=0.5}}, \tag{8}$$

where $f(\alpha)_{\alpha=0.5}$ represents a series of data plots at the given value of $\alpha = 0.5$, which is the control point of the reaction. The theoretical and experimental values of $\frac{d\alpha/d\theta}{(d\alpha/d\theta)_{\alpha=0.5}}$ were plotted against α . These values were compared to identify the theoretical reaction model for the HC mode with increasing temperature.

The analysis equation for the Friedman method [71], which is known to be the differential isoconversion method for determining the Arrhenius parameters, E_a and A , is derived from Equation (4):

$$\ln \frac{d\alpha}{dt} = \ln [A \cdot f(\alpha)] - \frac{E_a}{RT}. \tag{9}$$

Because the logarithmic term $\ln [A \cdot f(\alpha)]$ is constant for a given value of α , the plot of $\ln \frac{d\alpha}{dt}$ vs. $\frac{1}{T}$ can be used to derive a value for E_a from the gradient and a value for A from the intercept.

The sample temperature, T , at various reaction times t , can be determined using:

$$T = T_0 + \beta t, \quad \beta = \frac{dT}{dt}, \tag{10}$$

where T_0 and β correspond to the initiation temperature of the reaction and the constant rate of heating, respectively. Equation (4), under the conditions in Equation (10), is expressed in terms of the heating rate β as follows:

$$\frac{d\alpha}{dT} = \frac{A}{\beta} \cdot \exp\left(-\frac{E_a}{RT}\right) \cdot f(\alpha), \tag{11}$$

$$\ln\left(\beta \frac{d\alpha}{dT}\right) = \ln[A \cdot f(\alpha)] - \frac{E_a}{RT} \tag{11a}$$

The integration of Equation (11) leads to:

$$g(\alpha) = \int_0^\alpha \frac{d\alpha}{f(\alpha)} = \frac{A}{\beta} \int_{T_0}^T \exp\left(-\frac{E_a}{RT}\right) dT = \left[\frac{AE_a}{\beta R} p(x)\right]_{T_0}^T, \tag{12}$$

$$p(x) = \frac{\exp(-x)}{x(x+2)}, \quad x = \frac{E_a}{RT}, \tag{13}$$

where $p(x)$ is a function of Schlömilch series expansion. This is applicable for the condition $x \gg 15$, which is a first-order rational approximation [72]. Thus, the fraction conversion based on the model prediction can be estimated from Equations (12) and (13) and compared with that based on the experimental results.

3. Results and Discussion

3.1. Structural, Thermodynamic, Thermochemical, and Long-Term Thermal Stability

Figure 1a shows the XRD patterns of the long-term thermally cycled sample in the 2θ range. The black vertical bars below the XRD patterns indicate the peak positions of the samples. The peak positions were compared with the XRD data of the phase obtained from the COD standard database, and the phase of the sample was identified. A series of peaks corresponded to the bixbyite-type structure (COD ID 96-901-4249) (as denoted by the red vertical bars below the XRD pattern). No other peaks were observed in the pattern. This result indicates that after long-term thermal cycling, the sample was successfully maintained as a solid solution of $(\text{Mn}_{0.8}\text{Fe}_{0.2})_2\text{O}_3$ without impurities or thermodynamically unstable phases.

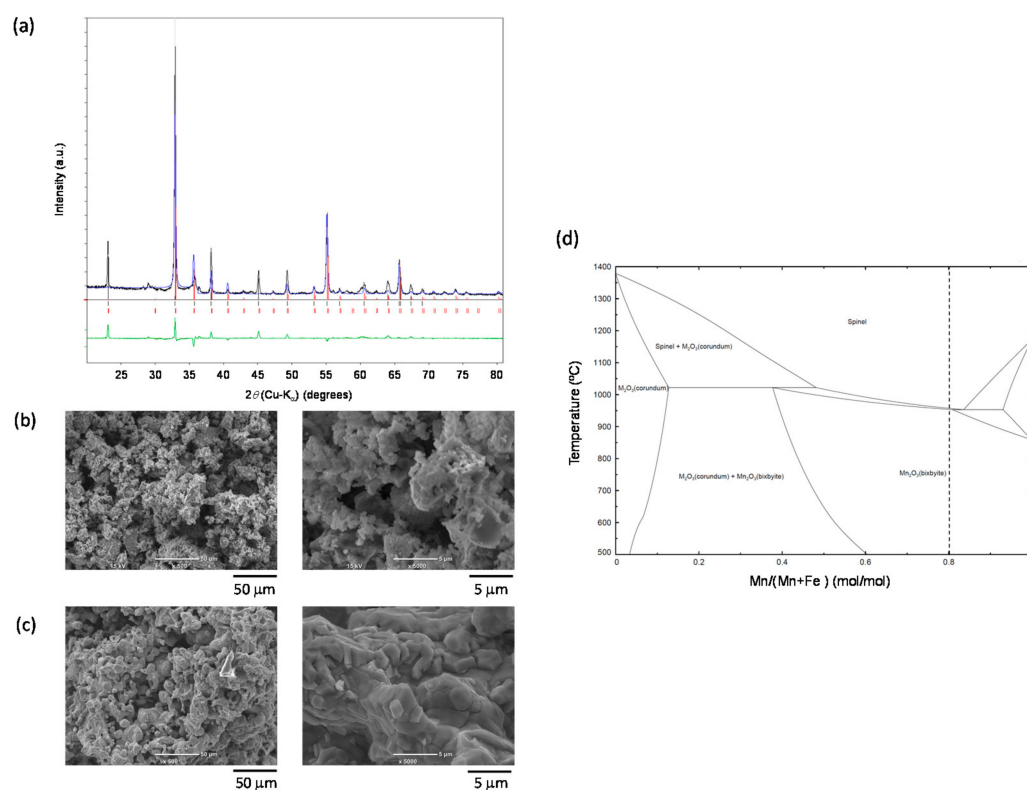


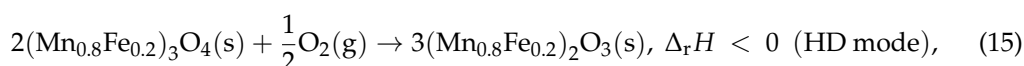
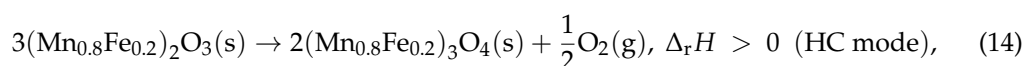
Figure 1. (a) XRD pattern of the Fe-substituted Mn_2O_3 sample obtained after the long-term cycling test. The green curve below the XRD patterns is a difference of intensity between experimental and Rietveld refinement of the structure model. (b) SEM images of the as-prepared sample. (c) SEM images of the sample obtained after the long-term test (360 runs of HC–HD cycle). (d) Phase diagram of the Mn-Fe-O system with an oxygen partial pressure of $P_{\text{O}_2} = 0.168$ bar.

Pure $\alpha\text{-Mn}_2\text{O}_3$ and $\alpha\text{-Fe}_2\text{O}_3$ have bixbyite- and corundum-type structures, respectively. Thus, not all possible solid solutions over all chemical compositions in the $\text{Mn}_2\text{O}_3\text{-Fe}_2\text{O}_3$ system are proportionally formed. However, the XRD results indicate that 20 mol% Fe_2O_3 can be successfully incorporated into the bixbyite-type structure as a solid solution, forming $(\text{Mn}_{0.8}\text{Fe}_{0.2})_2\text{O}_3$. The incorporation of Fe_2O_3 into Mn_2O_3 allows the Fe^{3+} ionic radius (low spin 0.55 Å; high spin 0.645 Å, with a coordination number of 6 with O^{2-} ions) to be equivalent to the Mn^{3+} ionic radius (0.58 Å, with a coordination number of 6 with O^{2-} ions) [73]. All diffraction peaks assigned to the solid-solution $(\text{Mn}_{0.8}\text{Fe}_{0.2})_2\text{O}_3$ phase were indexed, and the lattice cell parameters of the solid phase were evaluated via Rietveld refinement of the structure model. All peaks assigned to the solid-solution phase were indexed to cubic unit cells (space group I 21 3 (199)). The lattice parameters ($a = 9.421(1)$ Å) for the solid-solution phase were higher than those ($a = 9.410(0)$ Å) obtained in a previous

report for non-substituted $\alpha\text{Mn}_2\text{O}_3$ (COD ID 96-901-4249)). The results indicated that the Fe^{3+} ion in the solid solution of the long-term cycled sample was in the high-spin state. This is in good agreement with the fact that a series of peaks corresponding to the long-term cycled sample shifted to a lower diffraction angle than that of the non-substituted $\alpha\text{-Mn}_2\text{O}_3$.

The morphologies and particle sizes of the samples obtained after the as-prepared and long-term cycling tests were observed and evaluated in the secondary electron images (SEI; Figure 1b,c). As can be seen in Figure 1b, plate- and particle-like morphologies with angular and irregular shapes and widely dispersed particle sizes of 1–50 μm are shown for the as-prepared sample. The sample obtained after the long-term cycling test (Figure 1c) was compared with the as-prepared sample to confirm the coagulation and sintering of the particle-like samples subjected to high temperatures during the HC–HD cycle. The photograph at low magnification ($\times 500$, left side) shows that multiple round particles appear in the sample in the long-term cycling test. In addition, the particles coarsened and connected, similar to the three-dimensional shape of the porous body, compared to the as-prepared sample. In other words, the as-prepared sample did not change to a dense and hard mass after the long-term cycling tests. The morphological features allowing the passage of the gas phase in the 3D structure of the long-term cycled sample may provide long-term thermal stability at high temperatures during the HC–HD cycle. The photograph at high magnification ($\times 5000$, right side) shows that the coarsened small particles were fused, and large round-shaped secondary particles without micron-sized pores were formed in the long-term cycled sample. The size of the secondary particles was almost the same as that of the as-prepared samples. The results indicate that sintering of the primary particles during the HC–HD cycle was induced without the formation of dense and congested secondary particles.

A thermodynamic phase diagram of the Mn-Fe-O system (oxygen partial pressure of $P_{\text{O}_2} = 0.168$ atm) is shown in Figure 1d. The phase diagram was theoretically calculated using the thermodynamic equilibrium software program FactSage [74]. According to Figure 1d, $(\text{Mn}_{0.8}\text{Fe}_{0.2})_2\text{O}_3$ has a bixbyite structure with a thermodynamically stable phase at a low temperature ($T < 950$ °C) at a total pressure of 1 bar, while at a high temperature (950 °C $< T$) a structural phase transition takes place to the cubic spinel structure of $(\text{Mn}_{0.8}\text{Fe}_{0.2})_3\text{O}_4$. The characteristic feature of this chemical composition indicates that it is thermodynamically possible for the reversible phase transition between the two structures described above to occur without a region (or with a very narrow region) where the two phases co-exist. This was achieved using the swing temperature method in a gas stream with a constant oxygen partial pressure. The phase diagram indicates that the phase transition in the temperature range of 1050–700 °C (a lower limit temperature of 700 °C was installed from the viewpoint of transient rate change according to the course of time during the HC mode) can completely proceed, with both phases remaining thermodynamically stable. The reversible chemical reaction is expressed as follows:



where $(\text{Mn}_{0.8}\text{Fe}_{0.2})_2\text{O}_3$ was thermally reduced to produce $(\text{Mn}_{0.8}\text{Fe}_{0.2})_3\text{O}_4$ in HC mode. Oxygen is released through the external absorption of high-temperature heat in the endothermic process, whereas the reduced $(\text{Mn}_{0.8}\text{Fe}_{0.2})_3\text{O}_4$ is oxidized in an environmental atmosphere (oxygen) to return to $(\text{Mn}_{0.8}\text{Fe}_{0.2})_2\text{O}_3$, releasing the chemically stored heat to the gas stream. The gas stream plays two important roles, as the oxidant and HTF in the TCES system.

The reliability and long-term thermal stability of the HC–HD cycle for the sample were evaluated with a temperature swing of 1050–700 °C using TGA. The results are shown in Figure 2. As shown in Figure 2a, the signal of the DTA during the temperature swing decreases from the initial state by 5%, 7%, and 10% at the end of the 1st, 2nd, and

3rd sets, respectively. The DTA variation shifted toward relatively small variations as the run number increased during the 1st–3rd sets. The results indicate that the HC–HD performance of the sample gradually became stable and repeatable without significant degradation during temperature swings. The most likely reason for the weakening of the DTA signal may be one of the phenomena that evoke the sintering and coagulation of particles over cyclic HC and HD modes. A series of DTA hysteresis curves were compared to evaluate the variation in thermal performance, as shown in Figure 2b. The hysteresis curves for the 100th–360th cycles reveal that the endothermic and exothermic peaks lie in the ranges of 1264–1268 K and 1022–1026 K, respectively. Compared to those in the other cycles, the DTA hysteresis curves were stable and repeatable, showing identical peak positions in the HC–HD cycle. The results suggest that the sample can contribute to repeatable HC and HD modes over a long period during the temperature swing. To evaluate the oxygen release and uptake behavior, the mass change and mass change rate were plotted against the time in Figure 2c. The mass change was lower by 0.5%, 0.9%, and 1% at the end of the 1st, 2nd, and 3rd sets, respectively, whereas the mass change rate decreased from the initial value of 0.75%/min by 0.19%/min, 0.26%/min, and 0.30%/min for the 1st, 2nd, and 3rd sets, respectively. Both measures of change stabilized and became repeatable after the 1st set. The results show that the sample can provide repeatable HC and HD capacities over a long period.

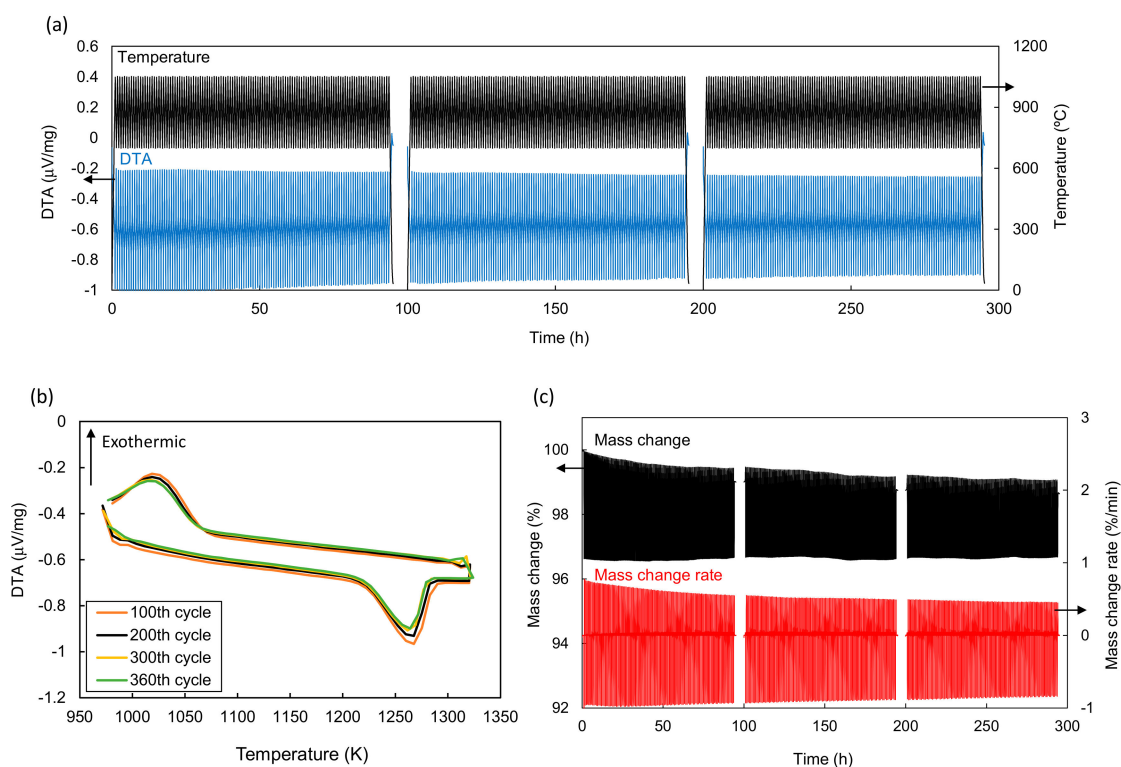


Figure 2. Long-term thermal stability of the HC–HD cycle with an oxygen partial pressure of $P_{O_2} = 0.168$ bar for the sample: variations in the (a) DTA signal, (b) hysteresis curve, and (c) mass change and mass change rate for the temperature swing.

3.2. Kinetic Analysis of HC Mode for Long-Term Cycled Sample

Figure 3a shows the variation in α with temperature during the HC mode. The HC mode was performed at five different heating rates (5–20 K/min) under a gas stream. As seen in Figure 3a, the phase transition of $(Mn_{0.8}Fe_{0.2})_2O_3$ to $(Mn_{0.8}Fe_{0.2})_3O_4$ at a heating rate of 5 K/min varies at a full-scale value of fractional conversion α , while that at the heating rates of 10–20 K/min changes in the range of $\alpha = 0.05$ –1.0. These results indicate that the temperature program of the TGA reactor can successfully acquire kinetic data

for the sample in the range of $\alpha = 0.05$ – 1.0 during the HC mode with different heating rates. The lack of kinetic data for $\alpha = 0$ – 0.05 may be due to the incomplete oxidation of the long-term cycled sample during the HD mode. As previously described, the sample had a morphological feature with a three-dimensional porous body, whereas the as-prepared sample formed an aggregation of fine and small particles (Figure 1). The structure of the long-term cycled sample enhances the thermal stability and repeatability of the HC–HD modes; however, it requires a long period of time (>2 h at 1073 K) for the complete oxidation of the sample during the HD mode.

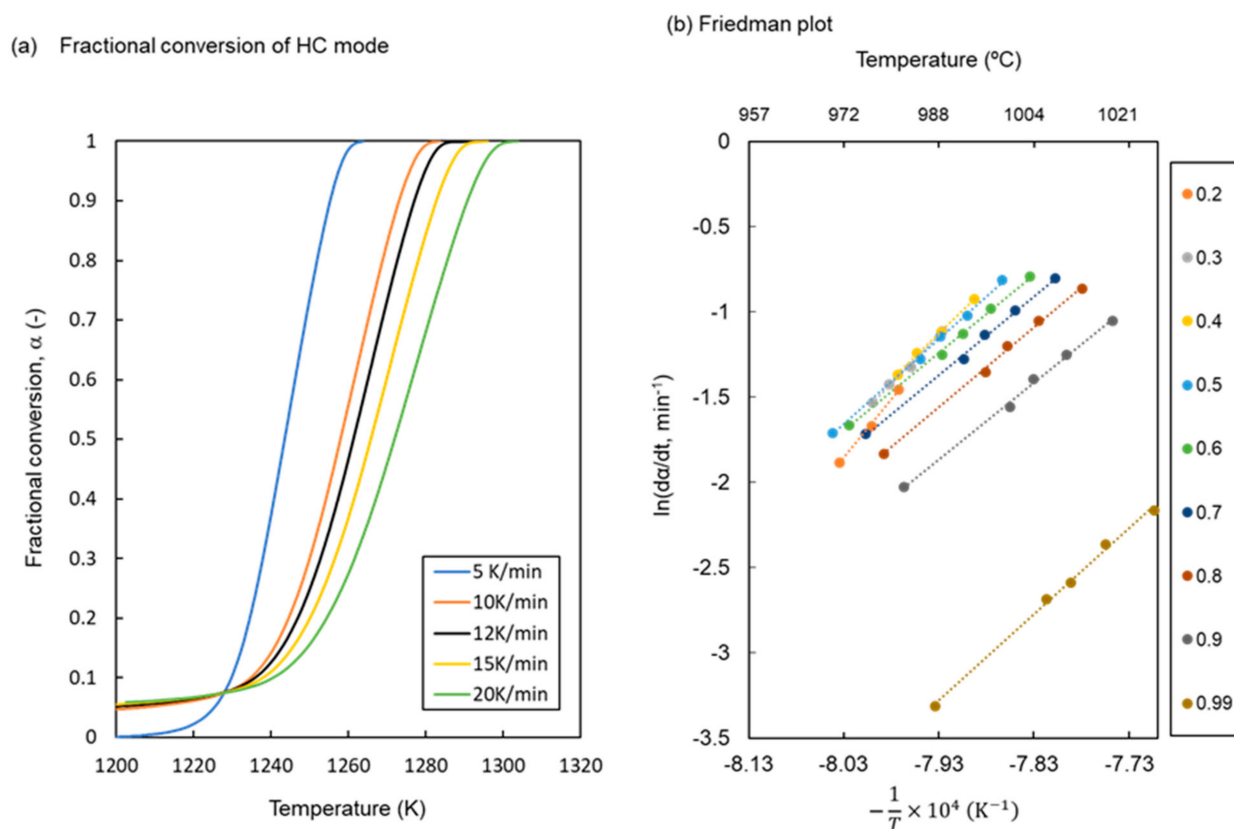


Figure 3. (a) Temperature variations in the fractional conversion of the long-term cycled sample during the HC mode. (b) Friedman plot of the long-term cycled sample to calculate the apparent activation energy against each value of the fractional conversion.

As shown in Figure 3a, the phase transition of $(\text{Mn}_{0.8}\text{Fe}_{0.2})_2\text{O}_3$ to $(\text{Mn}_{0.8}\text{Fe}_{0.2})_3\text{O}_4$ at heating rates of 5–20 K/min proceeds to completion in the gas stream until the temperature reaches 1300 K. In addition, the heating rates of 10–20 K/min did not affect the onset temperature of the HC mode, whereas the termination temperature of the HC mode shifted toward higher temperatures as the heating rate increased. These results indicate that the transition of $(\text{Mn}_{0.8}\text{Fe}_{0.2})_2\text{O}_3$ to $(\text{Mn}_{0.8}\text{Fe}_{0.2})_3\text{O}_4$ proceeds in a non-equilibrium state under the heating rates of the HC mode. Thus, the kinetic data for the mass change involved in the phase transition (with the release of O_2) during the HC mode were analyzed under heating rates to evaluate the thermochemical storage performance of the redox oxides. Figure 3b shows the Friedman plots of $(\text{Mn}_{0.8}\text{Fe}_{0.2})_2\text{O}_3$ for various values of α in order to determine E_a during the HC mode. The Friedman method was used to determine E_a according to Equation (9), without any assumptions regarding the reaction model function $f(\alpha)$, which represents the reaction mechanism. As seen in Figure 3b, all of the plots satisfy an approximately linear regression in the temperature range and follow the Arrhenius law. The tentative activation energies (E_a values) calculated from a set of straight lines are listed in Table S1 along with their correlation coefficient constants (R^2 values). The squares of

the correlation coefficient, R^2 , for the linear regression of the activation energy are in the range of 0.97–0.99. Figure 4 shows the variations in the apparent activation energy, E_a , with $\Delta\alpha = 0.01$ plotted against the α values. It appears that the value of E_a tends to gradually decrease with the increasing value of α in the first half of $\alpha = 0.20$ – 0.48 and stabilizes at almost the same level in the second half of the HC mode at $\alpha = 0.49$ – 1.0 . The values of the average activation energy were estimated to be $430.77 \text{ kJ}\cdot\text{mol}^{-1}$ in the full range of $\alpha = 0.11$ – 1.0 , $466.78 \text{ kJ}\cdot\text{mol}^{-1}$ in the first half and $389.22 \text{ kJ}\cdot\text{mol}^{-1}$ in the second half for the HC mode. The initial stage of $\alpha = 0$ – 0.20 was excluded from the estimation of the activation energy because of the large E_a fluctuation and relatively small R^2 values. The variations in E_a values indicate that the rate-determining step of the HC mode changes in the first and second halves of the HC mode. Thus, the authors attempted to verify the transition of the reaction mechanism during the HC mode and to examine the reaction model function $f(\alpha)$.

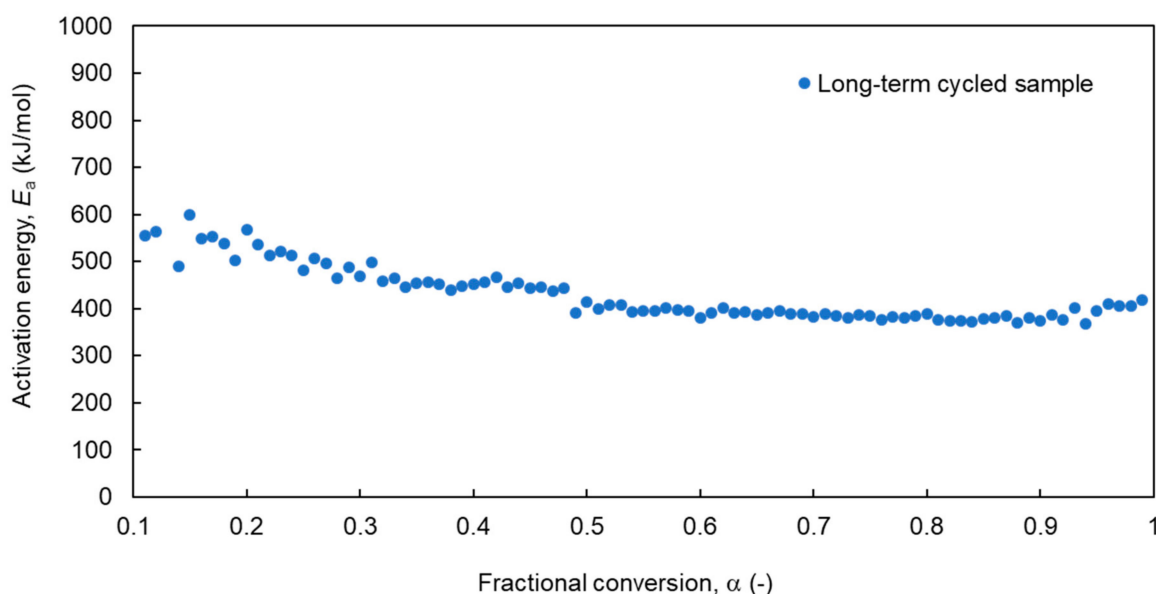


Figure 4. Variations in the apparent activation energy, E_a , of the long-term cycled sample against the fractional conversion of α during the HC mode. The values were calculated and plotted with $\Delta\alpha = 0.01$ to check the transition of the reaction model with progress of the reaction extent of the HC mode.

Several attempts have been made to determine the physicochemical mechanisms of solid-state reactions using the master plot method. Master plots refer to the theoretical reaction model function, $f(\alpha)$, which represents the reaction mechanism but is generally independent of the kinetic parameters (E_a and A) of the HC mode. In addition, theoretical master plots can be compared to experimental master plots calculated from kinetic data, allowing for the determination of an appropriate kinetic mechanism for the process. By combining a reaction model function $f(\alpha)$ that describes an appropriate kinetic mechanism with one of the kinetic parameters determined by the model-free method described above, the overall reaction rate equation can be formulated for the estimation of the HC performance in a thermochemical storage system.

Various theoretical reaction models based on the Arrhenius kinetic law have been proposed for the kinetic analysis of solid-state reactions [75,76]. These reaction models are listed in Table S2. In the present study, to determine the reaction model function $f(\alpha)$, master plots based on the differential forms of the generalized kinetic equation were applied. Figure 5 shows the master plot analysis of the sample during the HC mode when heated at (a) 5 K/min, (b) 10 K/min, (c) 12 K/min, (d) 15 K/min, and (e) 20 K/min. The theoretical master plots of $\frac{d\alpha/d\theta}{(d\alpha/d\theta)_{\alpha=0.5}}$ against α are compared with the experimental master plots of $\frac{d\alpha/d\theta}{(d\alpha/d\theta)_{\alpha=0.5}}$, calculated from the experimental data in Figure 3a. The general principle for

determining the reaction model function of the HC mode is to minimize the difference between the experimental and calculated kinetic data for the given reaction model function $f(\alpha)$ listed in Table S2. As shown in Figure 5, the possible theoretical models to fit the experimental data for all heating rates are the R2, A2, A3, and A4 models. As shown in Figure 5a, the experimental data appear to fit the A2 model at an initial stage of $\alpha = 0-0.20$ using visual pattern fitting, lying between the A2 and R2 models in the middle stage of $\alpha = 0.20-0.50$ and positioned on the A3 and R2 models in the middle-final stage of $\alpha = 0.50-1.0$. Alternatively, for heating rates of 10–20 K/min, it appears that the experimental data lie on the A2 model in the middle stage, while those on the R2 model lie in the middle-final stage. These results indicate that a method of visual pattern fitting is available for the selection of a possible model among the many candidates; however, it suffers due to the quantitative determination of the reaction model. Thus, we attempted to identify a well-described theoretical model using a statistical technique for making a simultaneous comparison between the theoretical and experimental models throughout the fractional conversion. The residual sum of squares (RSS) method was applied to quantitatively evaluate the difference between the experimental and estimated models:

$$\text{RSS} = \sum_{i=1}^n (y_i - \hat{y}_i)^2, \quad (16)$$

where n , y_i , and \hat{y}_i are the number of data points, value of the i th variable, and predicted value of the i th variable, respectively. A low RSS value indicates that the estimation model fits to the experimental model relatively well. The RSS values for several theoretical models at heating rates of 5–20 K/min are shown in Figure S1. As shown in Figure S1a, the RSS value for the A2 model for all heating rates is minimal and less than $\text{RSS} = 0.01$ in the range of $\alpha = 0.20-0.80$. As seen in Figure S1b, the RSS value for the R2 model for all heating rates decreases with increasing α values in the range of $\alpha = 0.20-0.40$, with minimal values in the range of $\alpha = 0.80-1.0$. In the range of $\alpha = 0.40-0.80$, both models can describe the reaction mechanism of the HC mode. Therefore, in terms of the variations in activation energy and the quantitative analysis of the model fit, it is concluded that the best estimates for the theoretical reaction model are the A2 and R2 models in the ranges of $\alpha = 0.20-0.48$ and $\alpha = 0.49-1.0$, respectively, in the HC mode.

From the results estimated for the activation energy E_a and the reaction model function $f(\alpha)$ mentioned above, the pre-exponential factor A can be calculated from the intercept of Equation (11a). Figure S2 shows the plots of the estimated pre-exponential factor A of the (a) A2 and (b) R2 models together with the standard deviation (SD, shown as error bars) against α for heating rates of 5–20 K/min during the HC mode. As shown in Figure S2a, the values of A for the heating rates of 10–20 K/min are almost the same regardless of the heating rate, and 8.38×10^{18} (1/min) on average. The value of A for a heating rate of 5 K/min was excluded from the estimation of A because of large deviations (17% from the average value) without a constant plateau (deviation of <0.4%) against the variation in heating rate. For the R2 model (Figure S2b), the estimated average of A for all heating rates was estimated as 3.15×10^{15} (1/min) as an independent function of the heating rate. Therefore, the rate equation for the thermal reduction kinetics of $(\text{Mn}_{0.8}\text{Fe}_{0.2})_2\text{O}_3$ during the HC mode in the gas stream is:

$$\begin{aligned} \text{A2 model; } \frac{d\alpha}{dt} = v_{\text{HC}} &= A \exp\left(-\frac{E_a}{RT}\right) \times 2(1-\alpha)[- \ln(1-\alpha)]^{\frac{1}{2}} \\ &= 8.38 \times 10^{18} \exp\left(-\frac{4.67 \times 10^5}{RT}\right) \times 2(1-\alpha)[- \ln(1-\alpha)]^{\frac{1}{2}}. \end{aligned} \quad (17)$$

$$\begin{aligned} \text{2 model; } \frac{d\alpha}{dt} = v_{\text{HC}} &= A \exp\left(-\frac{E_a}{RT}\right) \times 2(1-\alpha)^{\frac{1}{2}} \\ &= 3.15 \times 10^{15} \exp\left(-\frac{3.89 \times 10^5}{RT}\right) \times 2(1-\alpha)^{\frac{1}{2}}. \end{aligned} \quad (18)$$

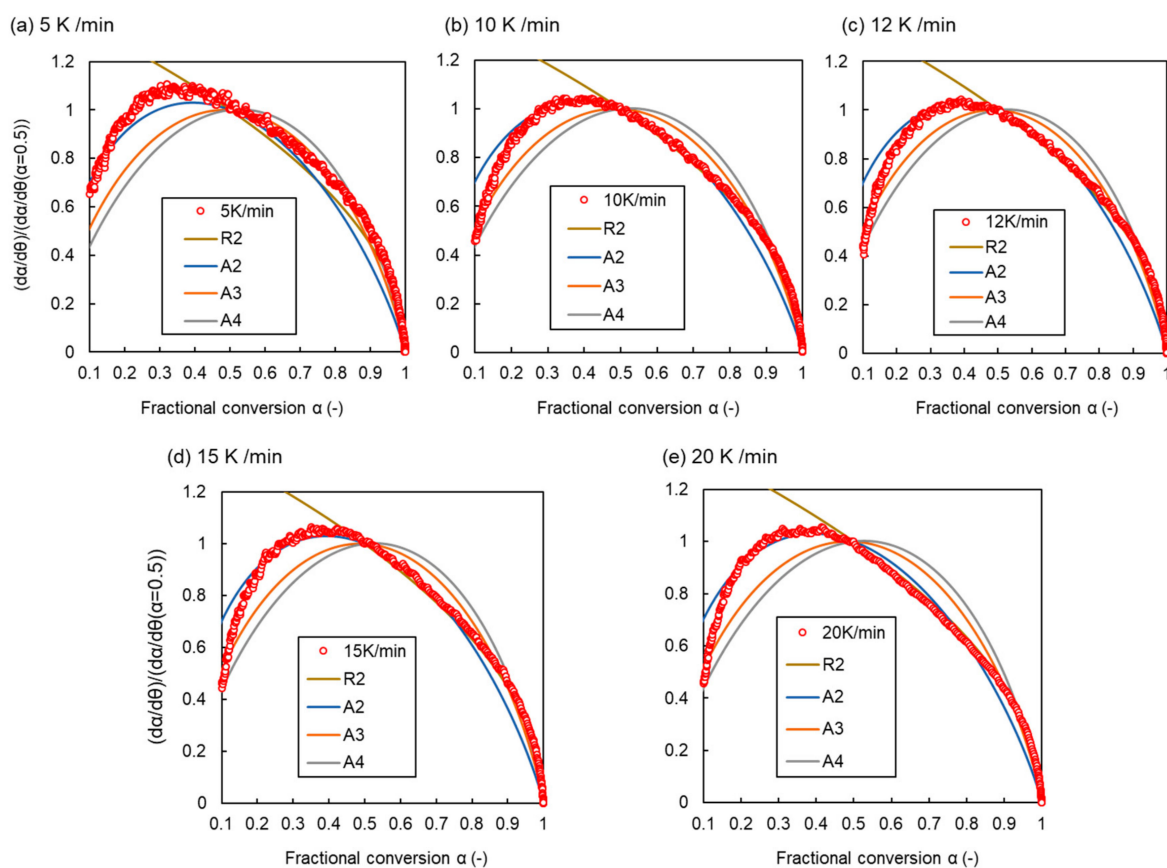


Figure 5. Master plots of the long-term cycled sample during the HC mode at heating rates of (a) 5 K/min, (b) 10 K/min, (c) 12 K/min, (d) 15 K/min, and (e) 20 K/min. Comparison of the experimental kinetic data (red circles) for the long-term cycled sample and possible reaction model (curves) against variations in the fractional conversion of α .

Figure 6 shows a comparison of the experimental fractional conversion and the fractional conversion estimated from the rate equation formulated in Equations (17) and (18), respectively. As seen in Figure 6a, it appears that for a heating rate of 5 K/min, the formulated A2 model fits well in the range of $\alpha = 0$ –0.20, while the formulated R2 model is in the range of $\alpha = 0.20$ –1.0. For the heating rates of 10–20 K/min, the A2 model in the initial stage of $\alpha = 0$ –0.20 shows similar behavior to the experimental data, while the difference between the experimental and theoretical conversion becomes smaller with increasing α values. However, the R2 model for all heating rates fits well with the experimental conversion in the middle–final stage of $\alpha = 0.50$ –1.0. These results indicate that the estimated predictive models for the heating rates in the gas stream are in good agreement with the experimental data. This proves the validity of the applied reaction model for describing the reductive kinetics of $(\text{Mn}_{0.8}\text{Fe}_{0.2})_2\text{O}_3$. The small deviation of the predicted conversion from the experimental data in the initial stage of $\alpha = 0$ –0.20 may be governed by the variable release behavior of the oxygen gas released from the surface of the sample and the diffusion mechanism of oxygen transportation in the sample due to the fluctuating activation energy.

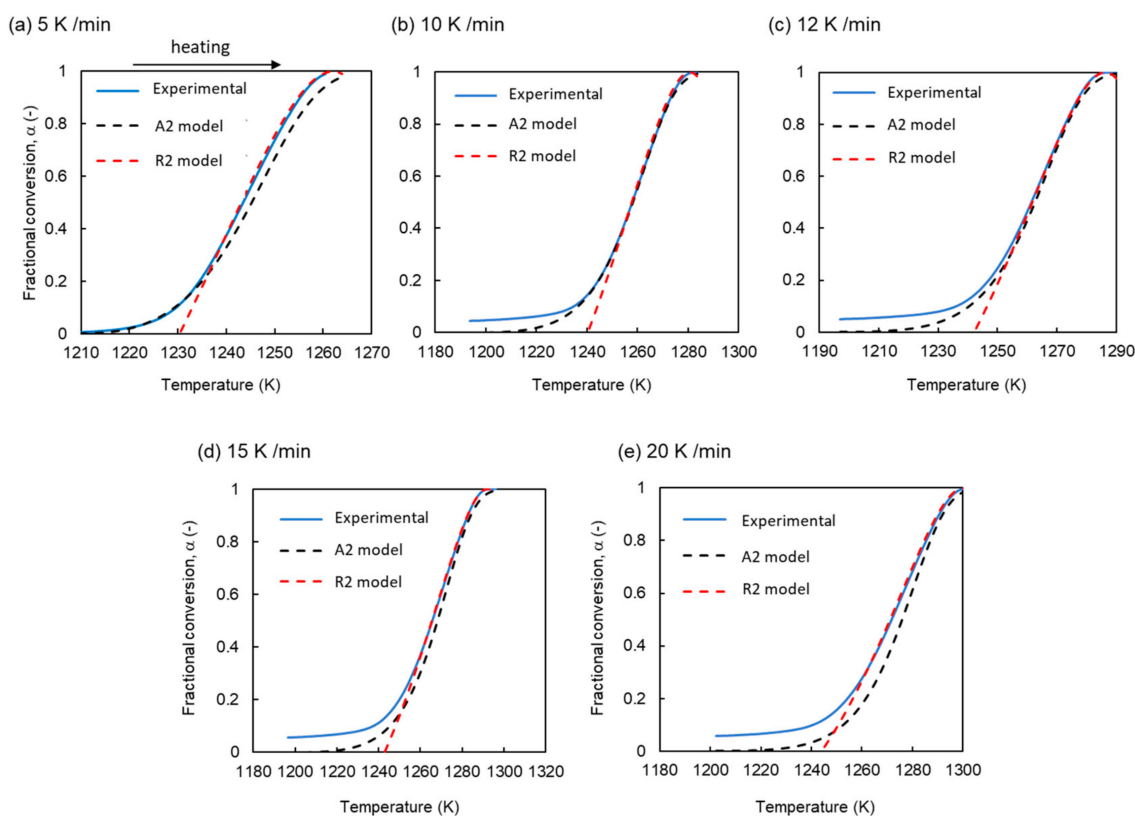


Figure 6. Temperature variation of the fractional conversion, α , of the long-term cycled sample during the HC mode for experimental (blue curve) and predicted reaction models (black and red curves for A2 and R2 models, respectively); the data of heating rate (a) 5 K/min, (b) 10 K/min, (c) 12 K/min, (d) 15 K/min, (e) 20 K/min. The curves are compared in these figures for the validation of the predicted reaction model.

3.3. Kinetic Analysis of the HC Mode for the As-Prepared Sample

The as-prepared Fe-substituted Mn_2O_3 was kinetically analyzed for the HC mode using the same methodology as that for the long-term cycled sample in Section 3.2. Figure 7a shows the variation in α with temperature during the HC mode. The phase transition of $(\text{Mn}_{0.8}\text{Fe}_{0.2})_2\text{O}_3$ to $(\text{Mn}_{0.8}\text{Fe}_{0.2})_3\text{O}_4$ at heating rates of 5–20 K/min proceeded to completion at temperatures of 1220–1300 K. In addition, the heating rates did not affect the onset temperature of the HC mode, whereas the termination temperature of the HC mode shifted toward higher temperatures as the heating rate increased. These results indicate that the transition of $(\text{Mn}_{0.8}\text{Fe}_{0.2})_2\text{O}_3$ to $(\text{Mn}_{0.8}\text{Fe}_{0.2})_3\text{O}_4$ in the as-prepared sample proceeds in a non-equilibrium state under the heating rates of the HC mode. The results in Figures 3a and 7a indicate that the heating rates tested in this study are a rate-determining step for the reaction rate of the HC mode, although the different morphologies of the samples due to their gas–solid contact may affect the extent of the HC mode. This may have been due to the configuration of the TGA equipment, which was composed of an upward gas stream and a solid sample mounted in the non-porous metallic cup.

Notably, except for the heating rate of 5 K/min, the data for α were initiated from $\alpha = 0.01$ (Figure 7a), whereas the values started from $\alpha = 0.05$ – 0.06 in the long-term cycled sample (Figure 3a). The results indicate that in comparison to the long-term cycled sample, the as-prepared sample has a suitable gas–solid contact and reversible reactivity during the HD mode in the TGA configuration.

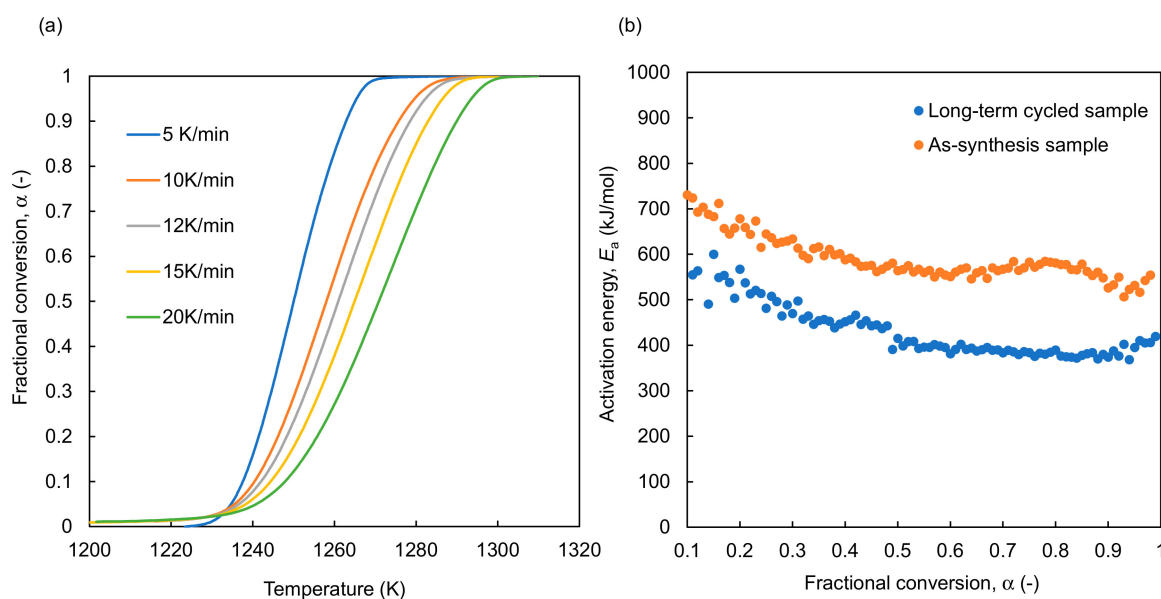


Figure 7. (a) Temperature variations in the fractional conversion of the as-prepared sample during the HC mode. (b) Variations in the apparent activation energy of the as-prepared sample against the fractional conversion. For comparison, the apparent activation energy of the long-term cycles sample is shown in this figure.

The kinetic data for the mass change involved in the phase transition with the release of O_2 during the HC mode were analyzed under heating rates to evaluate the thermochemical storage performance of the sample. Figure 7b shows a comparison of the activation energy variations between the as-prepared and long-term cycled samples. The E_a values of the as-prepared sample were higher over the entire range of α than those of the long-term cycled sample. The E_a value for the as-prepared sample tended to gradually decrease with increasing value of α in the first half of $\alpha = 0-0.45$ and plateaued in the second half of the HC mode of $\alpha = 0.46-1.0$. The variations were similar for both samples. The values of the average activation energy were estimated to be $600.61 \text{ kJ}\cdot\text{mol}^{-1}$ in the full range of $\alpha = 0-1.0$, $651.36 \text{ kJ}\cdot\text{mol}^{-1}$ in the first half and $560.40 \text{ kJ}\cdot\text{mol}^{-1}$ in the second half of the HC mode.

Figure 8a shows the master plot analysis of the as-prepared sample during the HC mode when heated at different rates of 5–20 K/min. Notably, in an initial stage of $\alpha = 0-0.15$, all theoretical models are not fitted in the experimental data for all heating rates in the as-prepared sample. A considerable reason is that a variation occurred in the morphology of the sample due to the coagulation and sintering of particles subjected to high temperatures during the initial stage of the HC mode, then multiple pathways of oxygen release within the sample were formed. This means that an oxygen release mechanism is not possible for a certain model in this stage of the HC mode. This assumption is supported by the results of the master plot for the long-term cycled sample, in which the morphology of the sample was stabilized at high temperatures. For the long-term cycled sample, the A2, A3, and A4 models were fitted to the experimental data with different heating rates in the initial stage (Figure 5). Except for the initial stage, the theoretical models needed for the as-prepared sample to fit the experimental data for all heating rates are the R3 and F1 models. To quantitatively evaluate the suitability of the experimental data against the fraction conversions for the estimated models, the RSS values for the R3 and F1 models are shown in Figure 8b,c. As seen in Figure 8b, the RSS value for the R3 model for heating rates of 10–20 K/min is in good agreement with the experimental data in the range of $\alpha = 0.15-1.0$. The experimental data for a heating rate of 5 K/min were fitted in the range of $\alpha = 0.30-1.0$. As shown in Figure 8c, the RSS values for the F1 model for all heating rates are less than $\text{RSS} = 0.01$ in the range of $\alpha = 0.35-1.0$. The results indicate that both models can

describe the reaction mechanism of the HC mode in the range of $\alpha = 0.30\text{--}1.0$. In addition, the experimental data in the range of $\alpha = 0.15\text{--}0.3$ desirably correspond to the R3 model.

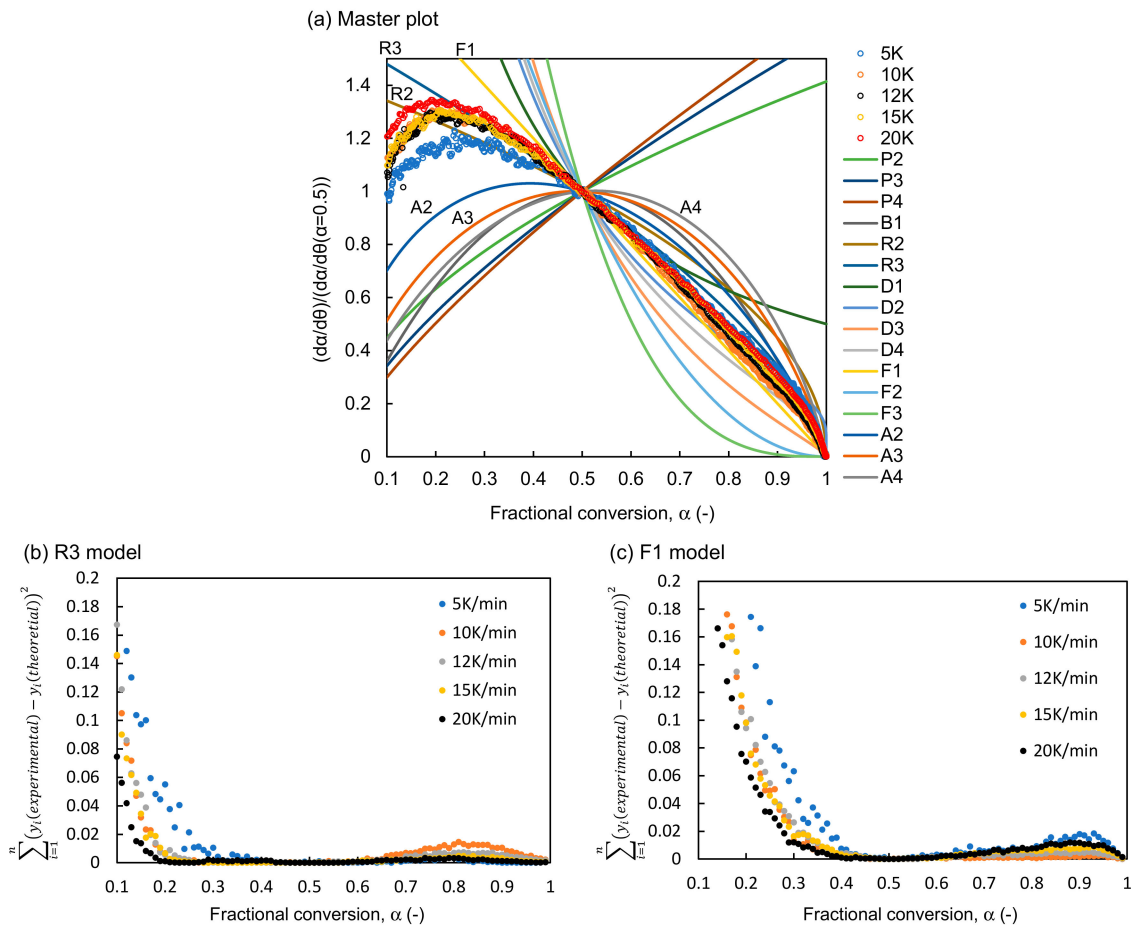


Figure 8. (a) Comparison of experimental kinetic data (circles) for the as-prepared sample and predicted reaction model (curves) against variations of fractional conversion of α . To estimate which reaction model fitted the experimental data, all possible theoretical models were examined. The RSS values of estimated (b) R3 and (c) F1 reaction models against variations of fractional conversion for all heating rates.

The pre-exponential factor A for the estimated R3 and F1 models can be calculated from the intercept of Equation (11a). Figure S3 shows the plots of the estimated pre-exponential factor A of the R3 and F1 models, together with the SD (shown as error bars) against α for all heating rates during the HC mode. As seen in Figure S3a, the values of A for the R3 model fluctuate with a large SD but are almost the same for all heating rates, with 7.28×10^{23} (1/min) on average. For the F1 model, the estimated average of A for all heating rates was estimated as 2.92×10^{24} (1/min) as an independent function of the heating rate (Figure S3b). Therefore, the rate equations for the HC mode of the as-prepared sample are:

$$\text{R3 model; } \frac{d\alpha}{dt} = A \exp\left(-\frac{Ea}{RT}\right) f(\alpha) = 7.28 \times 10^{23} \exp\left(-\frac{5.60 \times 10^5}{RT}\right) \times 3(1-\alpha)^{2/3} \quad (19)$$

$$\text{F1 model; } \frac{d\alpha}{dt} = A \exp\left(-\frac{Ea}{RT}\right) f(\alpha) = 2.92 \times 10^{24} \exp\left(-\frac{6.51 \times 10^5}{RT}\right) \times (1-\alpha) \quad (20)$$

Figure 9 shows the validation of the estimated R3 and F1 models of the rate equation formulated in Equations (19) and (20) compared with the experimental fractional conversions. It appears that in comparison to the F1 model, the formulated R3 model for all

heating rates fit well in the range of $\alpha = 0.15$ – 0.30 . In the range of $\alpha = 0.3$ – 1.0 , both models can equally describe the experimental data. These results indicate that the estimated predictive models of the HC mode are in good agreement with the experimental data for the as-prepared samples. This proves the validity of the applied reaction model for describing the reductive kinetics of $(\text{Mn}_{0.8}\text{Fe}_{0.2})_2\text{O}_3$. The small deviation in the predicted conversion from the experimental data in the initial stage of $\alpha = 0$ – 0.15 may be due to the higher activation energy than the average value and fluctuating pre-exponential factor, as well as the slow internal diffusion of the oxygen gas that was released in the sample mounted on the TGA equipment.

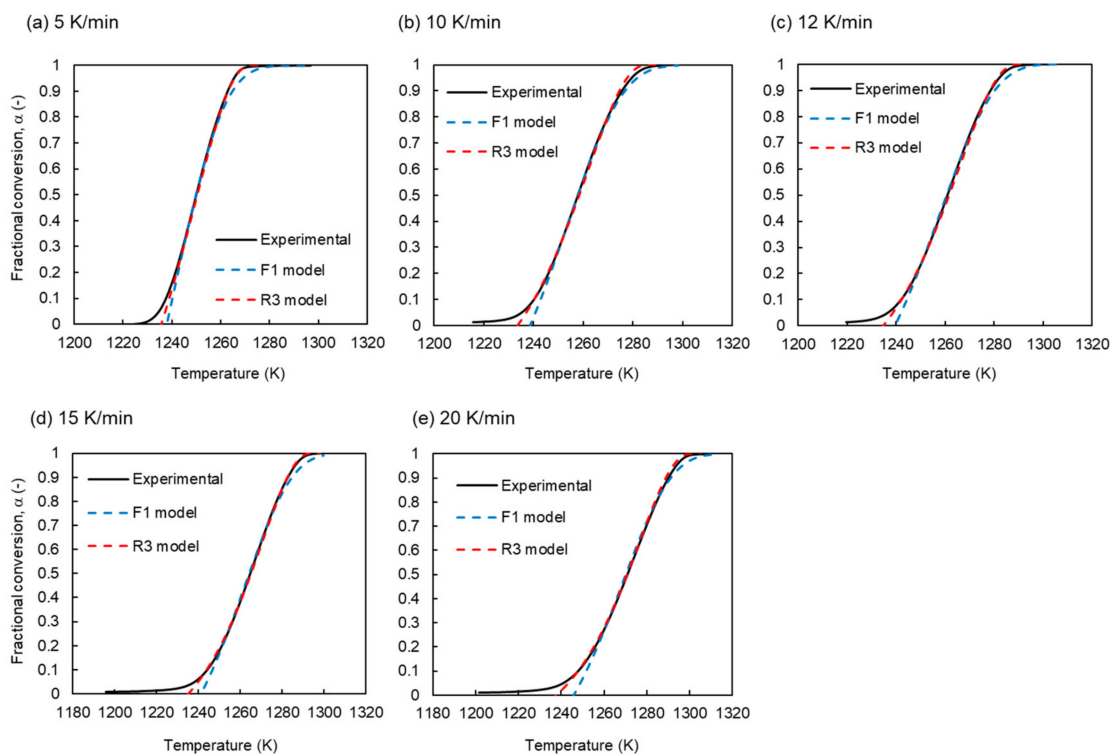


Figure 9. Temperature variation in the fractional conversion, α , of the as-prepared sample during the HC mode for experimental (black curve) and predicted reaction models (red and blue curves for R3 and F1 models, respectively); the data of heating rate (a) 5 K/min, (b) 10 K/min, (c) 12 K/min, (d) 15 K/min, (e) 20 K/min. The curves are compared in these figures for validation of the predicted reaction model.

From the viewpoint of the variation in the activation energy and the RSS values, it appears that for the as-prepared sample, the R3 model could describe the kinetics of the HC mode in the initial–middle stage of $\alpha = 0$ – 0.45 , while the models of both R3 and F1 could be explained in the range of $\alpha = 0.46$ – 1.0 .

3.4. Comparison with the Previous Kinetic Analysis of the HC Mode

The results of the kinetic analysis of the HC mode for the long-term cycled and as-prepared samples are compared with the previous kinetic analysis in Section 3.4. The chemical composition of the sample, the test conditions, and the previous kinetic data (estimated reaction model, activation energy, E_a , and pre-exponential factor, A) reported in the literature [65,66,77–80] are summarized in Table S3. The kinetic equations of the HC mode in the present and previous studies [68,69,80–83] are listed in Table 1. The kinetic data and equations for the non-substituted Mn_2O_3 samples were cited for comparison. The reaction models were estimated using different Fe substitution levels and atmospheres in previous studies. In the present study, the kinetics of $(\text{Mn}_{0.8}\text{Fe}_{0.2})_2\text{O}_3$ were formulated

and evaluated under an oxygen-containing gas stream ($P_{O_2} = 0.168$ bar), assuming that the samples were utilized as a thermochemical storage medium in a temperature swing process during the thermochemical HC and HD modes. The results for both samples in this study show that (1) the morphology of the sample can affect the kinetic behavior of the HC mode and (2) the rate-determining step of the HC mode can change with the progression of the reductive chemical reaction with the phase transition. Notably, the kinetic equations of the HC mode were evaluated under a specific gas–solid contact in the TGA equipment. In comparison with the results listed in Table S3, the chemical composition of the sample and test conditions (chemical composition and flow rate of the passing gas, P_{O_2} , temperature, and gas flow direction in the test equipment) are important factors governing the kinetics of the HC mode, releasing oxygen gas from the solid sample in a gas stream with an oxygen partial pressure at high temperatures.

Table 1. Kinetic equations of the HC mode for the present and previous studies using Fe-substituted Mn_2O_3 . The kinetic data for non-substituted Mn_2O_3 samples are listed as a comparison.

Material	Atmosphere	Reaction Model	Equation ($d\alpha/dt$)	References
As-prepared sample ($Mn_{0.8}Fe_{0.2}$) $_2O_3$	Air:N ₂ = 4:1	R3 ($\alpha = 0$ –1.0)	$\frac{d\alpha}{dt} = 7.28 \times 10^{23} \exp\left(-\frac{5.60 \times 10^5}{RT}\right) \times 3(1 - \alpha)^{2/3}$	Present study
		F1 ($\alpha = 0.46$ –1.0)	$\frac{d\alpha}{dt} = 2.92 \times 10^{24} \exp\left(-\frac{6.51 \times 10^5}{RT}\right) \times (1 - \alpha)$	
Long-term cycled sample ($Mn_{0.8}Fe_{0.2}$) $_2O_3$	Air:N ₂ = 4:1	A2 ($\alpha = 0.20$ –0.48)	$\frac{d\alpha}{dt} = 8.38 \times 10^{18} \exp\left(-\frac{4.67 \times 10^5}{RT}\right) \times 2(1 - \alpha)[- \ln(1 - \alpha)]^{1/2}$	Present study
		R2 ($\alpha = 0.49$ –1.0)	$\frac{d\alpha}{dt} = 3.15 \times 10^{15} \exp\left(-\frac{3.89 \times 10^5}{RT}\right) \times 2(1 - \alpha)^{1/2}$	
Mn_2O_3	N ₂	F1	$\frac{d\alpha}{dt} = 8.71 \times 10^9 \exp\left(-\frac{2.54 \times 10^5}{RT}\right) (1 - \alpha)$	[77]
($Mn_{0.8}Fe_{0.2}$) $_2O_3$	Ar	Sestak-Berggren (A3→A4)	$\frac{d\alpha}{dt} = 4.2 \times 10^{19} \exp\left(-\frac{3.71 \times 10^5}{RT}\right) \alpha^{1.75} \times (1 - \alpha)^{0.7} [- \ln(1 - \alpha)]^{-0.75}$	[65]
($Mn_{0.33}Fe_{0.67}$) $_2O_3$	Ar	D3	$\frac{d\alpha}{dt} = \frac{3.15 \times 10^{15}}{\beta} \exp\left(-\frac{426.13 \pm 0.04}{RT}\right) \frac{3(1 - \alpha)^{2/3}}{2[1 - (1 - \alpha)^{1/3}]} \times \left(1 - \frac{P_{O_2}}{P_{O_2,eq}}\right)^{25.01}$	[69]
($Mn_{0.75}Fe_{0.25}$) $_2O_3$	N ₂	A ($n =$ determined by exp)	$\frac{d\alpha}{dt} = 2.74 \times 10^{13} / s \exp\left(-\frac{3.56 \times 10^5}{RT}\right) \times 1.95(1 - X_{Red})[- \ln(1 - X_{Red})]^{(1 - \frac{1}{1.95})} \times \left(1 - \frac{P_{O_2}}{P_{O_2,eq}(T_{Red})}\right)^{4.55}$	[66]
Mn_2O_3	N ₂	A2	$\frac{d\alpha}{dt} = (1.72 - 1.80) \times 10^{18} / s \exp\left(-\frac{(2.68 - 2.81) \times 10^5}{RT}\right) \times 2(1 - \alpha)[- \ln(1 - \alpha)]^{1/2}$	[79]
	Air	A1.2	$\frac{d\alpha}{dt} = (8.09 - 9.12) \times 10^{18} / s \exp\left(-\frac{(1.03 - 1.37) \times 10^6}{RT}\right) \times 1.2(1 - \alpha)[- \ln(1 - \alpha)]^{1.2}$	
Mn_2O_3	Ar	D1	$\frac{d\alpha}{dt} = 1.39 \times 10^9 / s \exp\left(-\frac{3.62 \times 10^5}{RT}\right) \times \frac{1}{2\alpha}$	[80]

In the long-term cycle sample, the A2 model could explain the reductive kinetics of ($Mn_{0.8}Fe_{0.2}$) $_2O_3$ in the initial–middle stage, whereas the R2 model fit in the middle–final stage of the HC mode. The A_n model assumes a series of nucleation–growth processes as follows: (1) the formation of nuclei in a nucleation site; (2) growth and further nucleation; (3) an overlap of the nuclei; (4) ingestion of the nucleation site; (5) continued growth. The orders of nucleation are classified as A2, A3, or A4 to reflect the exponential terms in the reaction models shown in Table S2. The values of the exponent n for the A_n model indicate the different types of reaction mechanisms, as cited from the literature [81]. The A2 model obtained from the long-term cycled sample can be formally interpreted as an instantaneous random nucleation and two-dimensionally spread reductive reaction in the initial–middle reductive stage.

The geometric contraction models (R1–R3) assume that nucleation occurs rapidly on the surface of the solid. The reaction is controlled by the resulting reaction interface, progressing toward the center of the solid. Thus, different mathematical models have been derived for different solid shapes. When the solid particle was assumed to have a cylindrical shape, the contracting area (R2) model was employed, whereas when a spherical

or cubic shape was assumed, the contracting volume (R3) model was employed. The R2 model for the long-term cycled sample can be construed as the middle–final stage of the HC mode as follows: the nucleation and reaction proceed and spread within the contracting area of the cylindrical network structure with three-dimensionally connected particles.

In contrast, in the as-prepared sample, the R3 model could account for the reductive behavior over a very wide range of $\alpha = 0.15$ – 1.0 . In addition, the F1 model can explain in the range of $\alpha = 0.3$ – 1.0 . Owing to the morphology-forming agglomeration of particles with a spherical or cubic shape, nucleation occurs on the surfaces of the particles and the reductive reaction spreads inside the agglomeration (R3 model). In the reaction-order models (F0–F3), the reaction rate is proportional to the value of α , raised to a power that represents the reaction order. These types of models are the simplest of all kinetic models and are similar to those used in the homogeneous kinetics [75,76]. The F1 model is the simplest model, and it is similar to the homogeneous kinetics. The first-order model (F1), also called the Mampel model, is a special case of the A_n model, with $n = 1$. The solid–gas reaction processes involved in the thermal oxidation of porous silicon and desorption from the silica surface were reported to follow a first-order model [82,83].

4. Summary

The long-term thermal cycling stability of 20 mol% Fe-substituted Mn_2O_3 over 300 runs of thermochemical energy storage was studied using a temperature swing process to evaluate the repeatability and stability of the sample from the perspective of the microstructural characteristics and thermodynamic phase transitions. The kinetic analysis of the HC mode for the sample subjected to the long-term thermal cycling test with a temperature swing under a constant oxygen partial pressure was studied and compared with that of the as-prepared sample. Finally, the kinetic results in the present study were compared with the kinetic equations formulated under various test conditions in previous reports.

All of the diffraction peaks assigned to the $(Mn_{0.8}Fe_{0.2})_2O_3$ phase were indexed, and the lattice cell parameters of the solid phase were evaluated via Rietveld refinement of the structure model. The SEI photographs show a plate- and particle-like morphology with angular and irregular shapes for the as-prepared sample. In contrast, multiple round particles appeared in the sample used in the long-term cycling test. The particles coarsened and connected, similarly to the three-dimensional shape of the porous body, as compared to the as-prepared sample. The morphological features allowing the passage of the gas phase in the 3D structure of the long-term cycled sample may provide long-term thermal stability at high temperatures during the HC–HD cycle. According to the thermodynamic phase diagram of the Mn–Fe–O system, samples of the chemical composition enable the reversible phase transition between the bixbyite and spinel structures to occur without a region (or with a very narrow region) where the two phases co-exist. This is achieved using the swing temperature process in a gas stream containing oxygen. The reliability and long-term thermal stability of the HC–HD cycle for the samples were evaluated using TGA. These results imply that the sample can provide repeatable endothermic and exothermic capacities over a long duration.

The kinetics of the HC mode for the long-term cycled and as-prepared samples were analyzed using a combination of the Friedman and non-isothermal master plot methods to formulate the kinetic equation and describe the reaction mechanism by determining the appropriate reaction model. The RSS method was applied to identify the reaction model for both samples by evaluating quantitative differences between the experimental and estimated models. The RSS value for the long-term cycled sample was minimized for the A2 and R2 models at all heating rates. Therefore, from the viewpoint of the variations in the activation energy and quantitative analysis of model fitting, it is concluded that the best estimates for the theoretical reaction model are the A2 model in the range of $\alpha = 0.20$ – 0.48 and the R2 model in the range of $\alpha = 0.49$ – 1.0 during the HC mode.

The fractional conversions predicted from the rate equations formulated for both samples using the temperature swing method were in good agreement with the experimental data.

Supplementary Materials: The following supporting information can be downloaded at: <https://www.mdpi.com/article/10.3390/en15134812/s1>, Table S1. Tentative values of apparent activation energy of E_a and coefficient determination of R^2 for the long-term cycles sample during the HC mode. Table S2. Various theoretical reaction models for kinetic analysis of solid-state reactions. Table S3. Chemical composition of test material, test atmosphere, and kinetic data of HC mode for the present and previous studies using Fe-substituted Mn_2O_3 . The kinetic data for non-substituted Mn_2O_3 samples are listed as a comparison. Figure S1. The RSS values of estimated (a) A2 and (b) R2 reaction models against variations in fractional conversion during the HC mode at all heating rates. The experimental kinetic data of the long-term cycled sample are fitted to the estimated A2 and R2 reaction models. The RSS values are calculated. Figure S2. Relationship between pre-exponential factor, A , of (a) A2 model and (b) R2 model and heating rate, β , for the long-term cycled sample. Error bar of all plots is standard deviations in all fractional conversion ranges of $\alpha = 0-1.0$. Figure S3. Relationship between pre-exponential factor, A , of (a) R3 model and (b) F1 model and heating rate, β , for the as-prepared sample. Error bar of all plots is standard deviations in all fractional conversion ranges of $\alpha = 0-1.0$.

Author Contributions: N.G. contributed to the conceptualization, methodology, validation, formal analysis, writing—original draft preparation, writing—review and editing, supervision, project administration, funding acquisition, and provision of software and resources; K.H. and H.S. contributed to conducting the experiments and analysis, visualization, and data curation; F.O. contributed to the investigation and data curation. All authors have read and agreed to the published version of the manuscript.

Funding: This research was partially supported by the Ministry of Education, Culture, Sports, Science, and Technology, the Grand-in-Aid for Challenging Research (Exploratory), JSPS KAKENHI (Grant Number 21K18920); the Grant-in-Aid for Scientific Research (B), JSPS KAKENHI (Grant Number 22H02016); and the Grant-in-Aid for Scientific Research (C), JSPS KAKENHI (Grant Number 20K05398).

Data Availability Statement: The original contributions presented in the study are included in the article. Further inquiries can be directed to the corresponding author.

Acknowledgments: The authors gratefully acknowledge Tsuyoshi Hatamachi from the technical staff of the laboratory for acquiring the funding, together with N.G. and the supporting investigation and technical staff (Katsutoshi Iwafune) at Niigata University for supporting the XRD measurements, as well as the technical staff (Takahiro Nomoto) at Niigata University for supporting the SEM measurements.

Conflicts of Interest: The authors declare no conflict of interest.

References

1. Encinas-Sánchez, V.; Batuecas, E.; García, A.M.; Mayo, C.; Díaz, R.; Perez-Trujillo, F.J. Corrosion resistance of protective coatings against molten nitrate salts for thermal energy storage and their environmental impact in CSP technology. *Sol. Energy* **2018**, *176*, 688–697. [[CrossRef](#)]
2. Giglio, A.; Lanzini, A.; Leone, P.; García, M.M.R.; Moya, E.Z. Direct steam generation in parabolic-trough collectors: A review about the technology and a thermo-economic analysis of a hybrid system. *Renew. Sustain. Energy Rev.* **2017**, *74*, 453–473. [[CrossRef](#)]
3. Irwin, J.S.L.; Pfefferkorn, C.; Pitchumani, R. Thermochemical energy storage for concentrating solar thermal (CST) systems. In *Advances in Concentrating Solar Thermal Research and Technology*; Santigosa, L.R., Blanco, M.J., Eds.; Woodhead Publishing Series in Energy: Amsterdam, The Netherlands, 2016; pp. 247–266.
4. Panwar, N.L.; Kaushik, S.C.; Kothari, S. Role of renewable energy sources in environmental protection: A review. *Renew. Sustain. Energy Rev.* **2011**, *15*, 1513–1524. [[CrossRef](#)]
5. Arce, P.; Medrano, M.; Gil, A.; Oró, E.; Cabeza, L.F. Overview of thermal energy storage (TES) potential energy savings and climate change mitigation in Spain and Europe. *Appl. Energy* **2011**, *88*, 2764–2774. [[CrossRef](#)]
6. Kuravi, S.; Trahan, J.; Goswami, D.Y.; Rahman, M.M.; Stefanakos, E.K. Thermal energy storage technologies and systems for concentrating solar power plants. *Prog. Energy Combust. Sci.* **2013**, *39*, 285–319. [[CrossRef](#)]
7. Gil, A.; Medrano, M.; Martorell, I.; Lázaro, A.; Dolado, P.; Zalba, B.; Cabeza, L.F. State of the art on high temperature thermal energy storage for power generation. Part 1—Concepts, materials and modellization. *Renew. Sustain. Energy Rev.* **2010**, *14*, 31–55. [[CrossRef](#)]

8. 10 MW Solar Thermal Power Plant for Southern Spain; Final technical progress report for NNE5-1999-356 contract with the European Commission; European Union: Brussels, Belgium, 2006.
9. Kearney, D.; Kelly, B.; Herrmann, U.; Cable, R.; Pacheco, J.; Mahoney, R.; Price, H.; Blake, D.; Nava, P.; Potrovitza, N. Engineering aspects of a molten salt heat transfer fluid in a trough solar field. *Energy* **2004**, *29*, 861–870. [[CrossRef](#)]
10. Fernández, A.; Ushak, S.; Galleguillos, H.; Pérez, F. Development of new molten salts with LiNO_3 and $\text{Ca}(\text{NO}_3)_2$ for energy storage in CSP plants. *Appl. Energy* **2014**, *119*, 131–140. [[CrossRef](#)]
11. Rodríguez, I.; Pérez-Segarra, C.; Lehmkuhl, O.; Oliva, A. Modular object-oriented methodology for the resolution of molten salt storage tanks for CSP plants. *Appl. Energy* **2012**, *109*, 402–414. [[CrossRef](#)]
12. Chacartegui, R.; Vigna, L.; Becerra, J.; Verda, V. Analysis of two heat storage integrations for an Organic Rankine Cycle Parabolic trough solar power plant. *Energy Convers. Manag.* **2016**, *125*, 353–367. [[CrossRef](#)]
13. Kuravi, S.; Goswami, D.Y.; Stefanakos, E.K.; Ram, M.; Jotshi, C.; Pendyala, S.; Trahan, J.; Sridharan, P.; Rahman, M.; Krakow, B. (Eds.) Thermal energy storage for concentrating solar power plants. *Technol. Innov.* **2012**, *14*, 81–91. [[CrossRef](#)]
14. Karagiannakis, G.; Pagkoura, C.; Zygogianni, A.; Lorentzou, S.; Konstandopoulos, A. Monolithic Ceramic Redox Materials for Thermochemical Heat Storage Applications in CSP Plants. *Energy Procedia* **2014**, *49*, 820–829. [[CrossRef](#)]
15. González-Roubaud, E.; Pérez-Osorio, D.; Prieto, C. Review of commercial thermal energy storage in concentrated solar power plants: Steam vs. molten salts. *Renew. Sustain. Energy Rev.* **2017**, *80*, 133–148. [[CrossRef](#)]
16. Zalba, B.; Marin, J.M.; Cabeza, L.F.; Mehling, H. Review on thermal energy storage with phase change: Materials, heat transfer analysis and applications. *Appl. Therm. Eng.* **2003**, *23*, 251–283. [[CrossRef](#)]
17. Tian, Y.; Zhao, C. A review of solar collectors and thermal energy storage in solar thermal applications. *Appl. Energy* **2012**, *104*, 538–553. [[CrossRef](#)]
18. Do Couto Aktay, K.S.; Tamme, R.; Müller-Steinhagen, H. Thermal conductivity of high-temperature multicomponent materials with phase change. *Int. J. Thermophys.* **2008**, *29*, 678–692. [[CrossRef](#)]
19. Tamme, R. Trough Power Systems with Direct Steam Generation. In Proceedings of the Workshop on Thermal Storage for Trough Power Systems, Golden, CO, USA, 20–21 February 2003.
20. Zhao, C.; Opolot, M.; Liu, M.; Bruno, F.; Mancin, S.; Hooman, K. Numerical study of melting performance enhancement for PCM in an annular enclosure with internal-external fins and metal foams. *Int. J. Heat Mass Transf.* **2020**, *150*, 119348. [[CrossRef](#)]
21. Morisson, V.; Rady, M.; Palomo, E.; Arquís, E. Thermal energy storage systems for electricity production using solar energy direct steam generation technology. *Chem. Eng. Process. Process Intensif.* **2008**, *47*, 499–507. [[CrossRef](#)]
22. Birchenall, C.E.; Reichman, A.F. Heat-storage in eutectic alloys. *Metall. Trans. A* **1980**, *11*, 1415–1420. [[CrossRef](#)]
23. Khare, S.; Dell’Amico, M.; Knight, C.; McGarry, S. Selection of materials for high temperature latent heat energy storage. *Sol. Energy Mater. Sol. Cells* **2012**, *107*, 20–27. [[CrossRef](#)]
24. Zhang, G.; Li, J.; Chen, Y.; Xiang, H.; Ma, B.; Xu, Z.; Ma, X. Encapsulation of copper-based phase change materials for high temperature thermal energy storage. *Sol. Energy Mater. Sol. Cells* **2014**, *128*, 131–137. [[CrossRef](#)]
25. Zanganeh, G.; Khanna, R.; Walser, C.; Pedretti, A.; Haselbacher, A.; Steinfeld, A. Experimental and numerical investigation of combined sensible–latent heat for thermal energy storage at 575 °C and above. *Sol. Energy* **2015**, *114*, 77–90. [[CrossRef](#)]
26. Chacartegui, R.; Alovísio, A.; Ortiz, C.; Valverde, J.; Verda, V.; Becerra, J. Thermochemical energy storage of concentrated solar power by integration of the calcium looping process and a CO_2 power cycle. *Appl. Energy* **2016**, *173*, 589–605. [[CrossRef](#)]
27. Sánchez Jiménez, P.E.; Perejón, A.; Benítez Guerrero, M.; Valverde, J.M.; Ortiz, C.; Pérez Maqueda, L.A. High-performance and low-cost macroporous calcium oxide based materials for thermochemical energy storage in concentrated solar power plants. *Appl. Energy* **2019**, *235*, 543–552. [[CrossRef](#)]
28. Wong, B. *Thermochemical Heat Storage for Concentrated Solar Power*; Final Report; US Department of Energy: San Diego, CA, USA, 2011.
29. Generation 3 Concentrating Solar Power Systems (Gen3 CSP) Phase 3 Project Selection. 2021. Available online: <https://www.energy.gov/eere/solar/generation-3-concentrating-solar-power-systems-gen3-csp-phase-3-project-selection> (accessed on 10 June 2022).
30. Schwarzbözl, P.; Giuliano, S.; Noureldin, K.; Doerbeck, T.; Rosselló, A.; Schrüfer, J. Annual Performance Assessment of a 50 MWe Commercial Solar Tower Plant with Improved Open Volumetric Receiver. In Proceedings of the SolarPACES 2020, Online Event, 28 September–2 October 2020.
31. Fontalvo, A.; Guccione, S.; Wang, Y.; Wang, S.; Kee, Z.; Asselineau, C.-A.; Potter, D.; Venn, F.; Martinek, J.; Turchi, C.; et al. System-level comparison of sodium and salt systems in support of the Gen3 liquids pathway. *AIP Conf. Proc.* **2022**, *2445*, 030007. [[CrossRef](#)]
32. Coventry, J.; Andracka, C.; Pye, J.; Blanco, M.; Fisher, J. A review of sodium receiver technologies for central receiver solar power plants. *Sol. Energy* **2015**, *122*, 749–762. [[CrossRef](#)]
33. N’Tsoukpoe, K.E.; Liu, H.; Le Pierrès, N.; Luo, L. A review on long-term sorption solar energy storage. *Renew. Sustain. Energy Rev.* **2009**, *13*, 2385–2396. [[CrossRef](#)]
34. Fahim, M.; Ford, J. Energy storage using the BaO_2 BaO reaction cycle. *Chem. Eng. J.* **1983**, *27*, 21–28. [[CrossRef](#)]
35. Agrafiotis, C.; Roeb, M.; Sattler, C. Exploitation of thermochemical cycles based on solid oxide redox systems for thermochemical storage of solar heat. Part 4: Screening of oxides for use in cascaded thermochemical storage concepts. *Sol. Energy* **2016**, *139*, 695–710. [[CrossRef](#)]

36. Carrillo, A.J.; Sastre, D.; Serrano, D.P.; Pizarro, P.; Coronado, J.M. Revisiting the BaO₂/BaO redox cycle for solar thermochemical energy storage. *Phys. Chem. Chem. Phys.* **2016**, *18*, 8039–8048. [[CrossRef](#)]
37. Agrafiotis, C.; Roeb, M.; Schmücker, M.; Sattler, C. Exploitation of thermochemical cycles based on solid oxide redox systems for thermochemical storage of solar heat. Part 1: Testing of cobalt oxide-based powders. *Sol. Energy* **2014**, *102*, 189–211. [[CrossRef](#)]
38. Agrafiotis, C.; Tescari, S.; Roeb, M.; Schmücker, M.; Sattler, C. Exploitation of thermochemical cycles based on solid oxide redox systems for thermochemical storage of solar heat. Part 3: Cobalt oxide monolithic porous structures as integrated thermochemical reactors/heat exchangers. *Sol. Energy* **2015**, *114*, 459–475. [[CrossRef](#)]
39. Agrafiotis, C.; Roeb, M.; Schmücker, M.; Sattler, C. Exploitation of thermochemical cycles based on solid oxide redox systems for thermochemical storage of solar heat. Part 2: Redox oxide-coated porous ceramic structures as integrated thermochemical reactors/heat exchangers. *Sol. Energy* **2015**, *114*, 440–458. [[CrossRef](#)]
40. Block, T.; Knoblauch, N.; Schmücker, M. The cobalt-oxide/iron-oxide binary system for use as high temperature thermochemical energy storage material. *Thermochim. Acta* **2014**, *577*, 25–32. [[CrossRef](#)]
41. Pagkoura, C.; Karagiannakis, G.; Zygogianni, A.; Lorentzou, S.; Kostoglou, M.; Konstandopoulos, A.G.; Rattenbury, M.; Woodhead, J.W. Cobalt oxide based structured bodies as redox thermochemical heat storage medium for future CSP plants. *Sol. Energy* **2014**, *108*, 146–163. [[CrossRef](#)]
42. Karagiannakis, G.; Pagkoura, C.; Halevas, E.; Baltzopoulou, P.; Konstandopoulos, A.G. Cobalt/cobaltous oxide based honeycombs for thermochemical heat storage in future concentrated solar power installations: Multi-cyclic assessment and semi-quantitative heat effects estimations. *Sol. Energy* **2016**, *133*, 394–407. [[CrossRef](#)]
43. Schrader, A.J.; Muroyama, A.P.; Loutzenhiser, P.G. Solar electricity via an Air Brayton cycle with an integrated two-step thermochemical cycle for heat storage based on Co₃O₄/CoO redox reactions: Thermodynamic analysis. *Sol. Energy* **2015**, *118*, 485–495. [[CrossRef](#)]
44. Gokon, N.; Yokota, S.; Cho, H.S.; Hatamachi, T.; Kodama, T. Redox and fluidization performances of Co₃O₄/CoO for solar thermochemical energy storage. In Proceedings of the International Solar Energy Society/Solar World Congress 2015, Daegu, Korea, 8–12 November 2015.
45. Tescari, S.; Agrafiotis, C.; Breuer, S.; de Oliveira, L.; Neises-von Puttkamer, M.; Roeb, M.; Sattler, C. Thermochemical Solar Energy Storage Via Redox Oxides: Materials and Reactor/Heat Exchanger Concepts. *Energy Procedia* **2014**, *49*, 1034–1043. [[CrossRef](#)]
46. Neises, M.; Tescari, S.; de Oliveira, L.; Roeb, M.; Sattler, C.; Wong, B. Solar-heated rotary kiln for thermochemical energy storage. *Sol. Energy* **2012**, *86*, 3040–3048. [[CrossRef](#)]
47. Carrillo, A.J.; Moya, J.; Bayón, A.; Jana, P.; de la Peña O’Shea, V.A.; Romero, M.; Gonzalez-Aguilar, J.; Serrano, D.P.; Pizarro, P.; Coronado, J.M. Thermochemical energy storage at high temperature via redox cycles of Mn and Co oxides: Pure oxides versus mixed ones. *Sol. Energy Mater. Sol. Cells* **2014**, *123*, 47–57. [[CrossRef](#)]
48. Carrillo, A.J.; Serrano, D.P.; Pizarro, P.; Coronado, J.M. Thermochemical heat storage based on the Mn₂O₃/Mn₃O₄ redox couple: Influence of the initial particle size on the morphological evolution and cyclability. *J. Mater. Chem. A* **2014**, *2*, 19435–19443. [[CrossRef](#)]
49. Carrillo, A.J.; Serrano, D.P.; Pizarro, P.; Coronado, J.M. Manganese oxide-based thermochemical energy storage: Modulating temperatures of redox cycles by Fe–Cu co-doping. *J. Energy Storage* **2016**, *5*, 169–176. [[CrossRef](#)]
50. Carrillo, A.J.; Serrano, D.P.; Pizarro, P.; Coronado, J.M. Improving the thermochemical energy storage performance of the Mn₂O₃/Mn₃O₄ redox couple by the incorporation of iron. *ChemSusChem* **2015**, *8*, 1947–1954. [[CrossRef](#)]
51. Droege, P.; Carrillo, A.J.; Serrano, D.P.; Pizarro, P.; Coronado, J.M. Thermochemical heat storage at high temperatures using Mn₂O₃/Mn₃O₄ System: Narrowing the redox hysteresis by metal Co-doping. *Energy Procedia* **2015**, *73*, 263–271.
52. Gokon, N.; Nishizawa, A.; Yawata, T.; Bellan, S.; Kodama, T.; Cho, H.-S. Fe-doped manganese oxide redox material for thermochemical energy storage at high-temperatures. *AIP Conf. Proc.* **2019**, *2126*, 210003. [[CrossRef](#)]
53. Block, T.; Schmücker, M. Metal oxides for thermochemical energy storage: A comparison of several metal oxide systems. *Sol. Energy* **2016**, *126*, 195–207. [[CrossRef](#)]
54. Alonso, E.; Pérez-Rábago, C.; Licurgo, J.; Fuentealba, E.; Estrada, C.A. First experimental studies of solar redox reactions of copper oxides for thermochemical energy storage. *Sol. Energy* **2015**, *115*, 297–305. [[CrossRef](#)]
55. Babiniec, S.M.; Coker, E.N.; Miller, J.E.; Ambrosini, A. Doped calcium manganites for advanced high-temperature thermochemical energy storage. *Int. J. Energy Res.* **2015**, *40*, 280–284. [[CrossRef](#)]
56. Babiniec, S.M.; Coker, E.; Miller, J.E.; Ambrosini, A. Investigation of La_xSr_{1-x}Co_yM_{1-y}O_{3-δ} (M = Mn, Fe) perovskite materials as thermochemical energy storage media. *Sol. Energy* **2015**, *118*, 451–459. [[CrossRef](#)]
57. Imponenti, L.; Albrecht, K.J.; Braun, R.J.; Jackson, G.S. Measuring thermochemical energy storage capacity with redox cycles of doped-CaMnO₃. *ECS Trans.* **2016**, *72*, 11–22. [[CrossRef](#)]
58. Zhang, Z.; Andre, L.; Abanades, S. Experimental assessment of oxygen exchange capacity and thermochemical redox cycle behavior of Ba and Sr series perovskites for solar energy storage. *Sol. Energy* **2016**, *134*, 494–502. [[CrossRef](#)]
59. André, L.; Abanades, S.; Flamant, G. Screening of thermochemical systems based on solid-gas reversible reactions for high temperature solar thermal energy storage. *Renew. Sustain. Energy Rev.* **2016**, *64*, 703–715. [[CrossRef](#)]
60. Imponenti, L.; Albrecht, K.J.; Wands, J.W.; Sanders, M.; Jackson, G.S. Thermochemical energy storage in strontium-doped calcium manganites for concentrating solar power applications. *Sol. Energy* **2017**, *151*, 1–13. [[CrossRef](#)]

61. Galinsky, N.; Mishra, A.; Zhang, J.; Li, F. $\text{Ca}_{1-x}\text{A}_x\text{MnO}_3$ (A = Sr and Ba) perovskite based oxygen carriers for chemical looping with oxygen uncoupling (CLOU). *Appl. Energy* **2015**, *157*, 358–367. [CrossRef]
62. Albrecht, K.J.; Jackson, G.S.; Braun, R.J. Thermodynamically consistent modeling of redox-stable perovskite oxides for thermochemical energy conversion and storage. *Appl. Energy* **2016**, *165*, 285–296. [CrossRef]
63. Vieten, J.; Bulfin, B.; Call, F.; Lange, M.; Schmücker, M.; Francke, A.; Roeb, M.; Sattler, C. Perovskite oxides for application in thermochemical air separation and oxygen storage. *J. Mater. Chem. A* **2016**, *4*, 13652–13659. [CrossRef]
64. Gokon, N.; Yawata, T.; Bellan, S.; Kodama, T.; Cho, H.S. Thermochemical behavior of perovskite oxides based on $\text{La}_x\text{Sr}_{1-x}(\text{Mn}, \text{Fe}, \text{Co})\text{O}_{3-\delta}$ and $\text{Ba}_y\text{Sr}_{1-y}\text{CoO}_{3-\delta}$ redox system for thermochemical energy storage at high temperatures. *Energy* **2019**, *171*, 971–980. [CrossRef]
65. Carrillo, A.J.; Serrano, D.P.; Pizarro, P.; Coronado, J.M. Understanding Redox Kinetics of Iron-Doped Manganese Oxides for High Temperature Thermochemical Energy Storage. *J. Phys. Chem. C* **2016**, *120*, 27800–27812. [CrossRef]
66. Wokon, M.; Block, T.; Nicolai, S.; Linder, M.; Schmücker, M. Thermodynamic and kinetic investigation of a technical grade manganese-iron binary oxide for thermochemical energy storage. *Sol. Energy* **2017**, *153*, 471–485. [CrossRef]
67. Wokon, M.; Kohzer, A.; Linder, M. Investigations on thermochemical energy storage based on technical grade manganese-iron oxide in a lab-scale packed bed reactor. *Sol. Energy* **2017**, *153*, 200–214. [CrossRef]
68. André, L.; Abanades, S.; Cassayre, L. High-temperature thermochemical energy storage based on redox reactions using Co-Fe and Mn-Fe mixed metal oxides. *J. Solid State Chem.* **2017**, *253*, 6–14. [CrossRef]
69. Hamidi, M.; Bayon, A.; Wheeler, V.M.; Kreider, P.; Wallace, M.A.; Tsuzuki, T.; Catchpole, K.; Weimer, A.W. Reduction kinetics for large spherical 2:1 iron–manganese oxide redox materials for thermochemical energy storage. *Chem. Eng. Sci.* **2019**, *201*, 74–81. [CrossRef]
70. Li, C.; Tang, T.B. Isoconversion method for kinetic analysis of solid-state reactions from dynamic thermoanalytical data. *J. Mater. Sci.* **1999**, *34*, 3467–3470. [CrossRef]
71. Friedman, H.L. Kinetics of thermal degradation of char-forming plastics from thermogravimetry. Application to a phenolic plastic. *J. Polym. Sci. Polym. Symp.* **1964**, *6*, 183–195. [CrossRef]
72. Flynn, J.H. The ‘Temperature Integral’—Its use and abuse. *Thermochim. Acta* **1997**, *300*, 83–92. [CrossRef]
73. Shannon, R.D. Revised effective ionic radii and systematic studies of interatomic distances in halides and chalcogenides. *Acta Cryst.* **1976**, *32*, 751–766. [CrossRef]
74. Factsage, GTT-Technologies Kaiserstrasse 100, 52134 Herzogenrath, GERMANY. Available online: <http://www.gtt-technologies.de/> (accessed on 10 June 2022).
75. Khawam, A.; Flana, D.R. Solid-state kinetic models: Basics and mathematical fundamentals. *J. Phys. Chem. B* **2006**, *110*, 17315–17328. [CrossRef]
76. Fedunik-Hofman, L.; Bayon, A.; Donne, S.W. Kinetics of Solid-Gas Reactions and Their Application to Carbonate Looping Systems. *Energies* **2019**, *12*, 2981. [CrossRef]
77. Botas, J.A.; Marugán, J.; Molina, R.; Herradón, C. Kinetic modelling of the first step of $\text{Mn}_2\text{O}_3/\text{MnO}$ thermochemical cycle for solar hydrogen production. *Int. J. Hydrog. Energy* **2012**, *37*, 18661–18671. [CrossRef]
78. Carrillo, A.J.; Pizarro, P.; Coronado, J.M. Assessing Cr incorporation in $\text{Mn}_2\text{O}_3/\text{Mn}_3\text{O}_4$ redox materials for thermochemical heat storage applications. *J. Energy Storage* **2021**, *33*, 102028. [CrossRef]
79. Li, L.; He, M.; Zhang, A.; Zhou, J. A study on non-isothermal kinetics of the thermal decompositions of β -manganese dioxide. *Thermochim. Acta* **2011**, *523*, 207–213. [CrossRef]
80. Alonso, E.; Romero, M. A directly irradiated solar reactor for kinetic analysis of non-volatile metal oxides reductions. *Int. J. Energy Res.* **2015**, *39*, 1217–1228. [CrossRef]
81. Pérez-Maqueda, L.; Criado, J.; Málek, J. Combined kinetic analysis for crystallization kinetics of non-crystalline solids. *J. Non-Cryst. Solids* **2003**, *320*, 84–91. [CrossRef]
82. Pap, A.E.; Kordás, K.; George, T.F.; Leppävuori, S. Thermal Oxidation of Porous Silicon: Study on Reaction Kinetics. *J. Phys. Chem. B* **2004**, *108*, 12744–12747. [CrossRef]
83. Carniti, P.; Gervasini, A.; Bennici, S. Experimental and Modelization Approach in the Study of Acid-Site Energy Distribution by Base Desorption. Part I: Modified Silica Surfaces. *J. Phys. Chem. B* **2005**, *109*, 1528–1536. [CrossRef] [PubMed]